Quantitative Studies of Microstructural Phase Transformation:
Critical Features of Nickel Titanium Polycrystals Undergoing Superelastic Deformation

by

Michael Gregory Kimiecik

A dissertation submitted in partial fulfillment
of the requirements for the degree of
Doctor of Philosophy
(Materials Science and Engineering)
in The University of Michigan
2015

Doctoral Committee:

    Professor J. Wayne Jones, Co-Chair
    Associate Professor Samantha Daly, Co-Chair
    Associate Professor Emmanuelle Marquis
    Professor John Shaw

DEDICATION

To the ones who made this possible

and the one who made me want it.

I also enjoyed the support of my family back in California, who never rubbed the discrepancy in winter weather in my face. Thank you to Kenneth, Karin, Robert and Sarah Kimiecik as well as Kay, Tess, and Skylar Brooks.

Lastly I would like to thank my better half for her love and support through all the difficulties a PhD brings about. I am lucky that our paths crossed when they did and that they have been entangled from that day forward. All of this would have been impossible without you, Meegan Bay Brooks.

TABLE OF CONTENTS

LIST OF FIGURES

ABSTRACT

This dissertation addresses the stress-induced phase transformation that occurs upon the loading of Nickel-Titanium alloys, leading to their superelastic properties. Superelasticity is widely utilized in biomedical applications including stents and valves, but there is still much that is unknown regarding the interaction between the superelastic martensitic transformation and microstructure of these materials. To help fill this knowledge gap, an experimental technique combining high resolution Scanning Electron Microscopy and Digital Image Correlation was applied to the analysis of superelastic nickel titanium shape memory alloy. The displacement and subsequent strain maps generated from this technique, combined with crystallographic orientation gathered via Electron Backscatter Diffraction, allowed the tracking of subgrain martensite transformation in polycrystalline specimens. Additional analytical tools were developed to determine the configuration of martensite variants in each transformed grain. These observations provide new details on how the macroscopic martensite band progresses through polycrystals and how that martensite is configured in the transformed martensite band. The previously held assumption that in a superelastic polycrystal similarly oriented grains transform similarly is found to be inaccurate based on experimental observations. Previously unobserved lattice correspondence variant configurations of martensite were found to readily develop in the polycrystalline specimens in addition to the previously observed habit plane variants. The appearance of these correspondence variant configurations was due to the large resolved shear stress on twin planes as identified using logistic regression on the configuration fractions and the underlying grain orientations of the polycrystal. Those areas which primarily transformed to

correspondence variant configurations accumulated an increased amount of residual strain, which served as a blueprint for subsequent transformation. While the interaction between martensite, plasticity, and polycrystalline microstructures requires more work to fully characterize, this dissertation represents an attempt to understand the complex interactions taking place in superelastic material undergoing cyclic loading.

CHAPTER 1: INTRODUCTION AND BACKGROUND LITERATURE

Shape memory alloys (SMAs) exhibit two unique properties arising from a solid-to-solid, diffusionless phase transformation: the shape memory effect and superelasticity [1]. Both properties allow SMAs to recover large strains with little residual deformation and stem from a phase transformation between an austenite phase and one or more martensite variants (Figure 1.1). Superelastic deformation in the nickel-titanium SMA, which is the focus of this work, proceeds by a transition from a parent phase with a B2 crystal structure to a single variant, or twinned variant pair, of a B19′ structure that accommodates the applied strain. Recovery occurs upon unloading through reverse transformation to the thermodynamically stable austenite phase. Modeling of the crystallographic influences of this transformation has been considered on a number of length scales, from the macroscale stress-strain response of single or textured polycrystalline samples to the microscale measurement of transformation within individual grains. However, an empirical analysis of transformation on smaller length scales to test the accuracy of these analytical models has not yet been achieved.

This chapter provides a review of the basics of martensite transformation in the Ni-Ti SMA for macroscopic specimens, single crystals, and polycrystals. The objective of the review is to examine the current state of research in martensite transformation of shape memory alloys, and the shortcomings that need to be addressed in order to improve our understanding of the phenomenon.

The review will start with an overview of the macroscopic characterization of martensitic transformation and its associated phenomenological theories. A review is also included of the mathematical formalism required to describe the compatibility requirements of martensite and

austenite interfaces. A summary of experiments that measured martensite transformation in single crystals, and the extension of those results to models of polycrystalline transformation, is also presented. These predictions will be compared against experiments on polycrystalline SMA, and the limitations in extending single crystal results to polycrystalline SMAs will be addressed. Lastly, the cyclic deformation of SMAs will be discussed to provide background on the low cycle fatigue tests performed in this dissertation research.

SECTION 1.1: BASICS OF MACROSCOPIC MARTENSITE TRANSFORMATION

There is an extensive body of work characterizing the heterogeneity involved with the martensitic transformation at the macroscopic length scale (for example, see [2,3] and the references contained therein), but few measurements have been made of transformation at length scales on the order of the grain size or smaller. Multiple techniques have shown that at the macroscale, Lüders-like band structures of localized martensite nucleate and propagate to accommodate strain in a specimen under tensile loading at relatively low strain rates [4–9]. Depending on the particular sample geometry, the bands can appear to be a flat interface moving along the length of thin wire [10–13], an angled band that grows in width across the face of a thin sheet [4–9,14–16], or several bands which spiral up a thin-walled tube [17–19].

Low strain rates (10^{-5} to 10^{-4} sec^{-1}) are important to avoid the temperature rise associated with latent heat release, which will affect transformation behavior [14,20,21]. Strain rates on the order of 10^{-3} sec^{-1} or higher can cause local heating around the martensite band, increasing the stress required (described by the Clausius–Clapeyron relationship) for continued propagation of the band, which makes it more energetically favorable for bands to nucleate elsewhere in the sample.

Initially, these macroscopically martensite bands were regarded as monolithic structures composed of favorable martensite variants with a sharp transition—defined by a crystallographic habit plane—between the transformed and untransformed regions. However, recent investigations [17,22–28] have shown that the bands are not monolithic, nor are they comprised solely of favorable martensitic variants. Rather, at the microscale a single martensite band consists of a complex array of interacting variants and has no clearly defined boundary with the untransformed material. The details of how these variants are arranged and distributed throughout a polycrystalline microstructure is an area of current research.

SECTION 1.2: CRYSTALLOGRAPHY AND PHENOMENOLOGICAL THEORY OF MARTENSITE

TRANSFORMATION

The transformation from austenite to martensite in nickel titanium is a diffusionless transition from a cubic B2 to monoclinic B19′ crystal structure. Due to the lower symmetry of the martensite compared to its parent austenite, this transformation can take on many different configurations, or Correspondence Variants (CVs), depending on the orientation of the martensite in reference to the parent austenite. [1,29–32] For the B2 to B19′ transformation there are 12 equivalent orientations of CVs. Each orientation induces a net stretch, which can be represented as the Bain matrix

$$\boldsymbol{U}_1 = \begin{bmatrix} \gamma & \epsilon & \epsilon \\ \epsilon & \alpha & \delta \\ \epsilon & \delta & \alpha \end{bmatrix} \tag{1.1}$$

where: γ=0.9563, ϵ= -0.0427, α=1.0243, and δ=0.058. [31] From this principal CV, the other 11 can be found by applying the rotations $\boldsymbol{R}_i$ from the cubic symmetry group $\mathcal{L}_{cubic}$ to the parent austenite prior to transformation and then reversing the transformation such that each other martensite variant can be represented as

$$U_i = R_i^T U_1 R_i \tag{1.2}$$

The parameters of the Bain matrix yield a maximum volume change from austenite to martensite of 0.334%, which is relatively small.

One characteristic of the martensitic transformation in nickel titanium is the lack of direct compatibility between the austenite and martensite phases. [1,31] To be compatible, the transformed martensite, U_i, with a rotation, Q, must satisfy the condition that for some habit plane normal, $\hat{m}$, and shear direction, b, in that plane

$$QU_i - I = b \otimes \hat{m} \tag{1.3}$$

For nickel titanium no solution for this compatibility exists for the single-phase compositions of martensite. However, compatibility between the austenite and martensite phases can be achieved if the martensite arranges in particular configurations (see Figure 1.2). Specifically, the martensite can be twinned in a particular volume fraction ratio to produce an effective Bain matrix to satisfy the compatibility condition. To form a twin, two variants, U_i and U_j, of martensite must satisfy

$$QU_i - U_j = a \otimes \hat{n} \tag{1.4}$$

where $\hat{n}$ is the twin plane normal, a is the twin shear direction, and Q is again a rotation of one martensite variant. The relationship of a and $\hat{n}$ to the symmetry directions of $\mathcal{L}_{cubic}$ determine the twin type. Twins with twin planes that are also symmetry planes of $\mathcal{L}_{cubic}$ are referred to as Type I twins, while twins with shear directions parallel to the symmetry plane normal are Type II twins. If such a twin can form, then it is possible to test its compatibility with the parent austenite by constructing a new effective Bain matrix, U_{HPV}, for the twinned structure based on the volume fraction, λ, of one of its variants.

$$U_{HPV} = \lambda QU_i + (1 - \lambda)U_j \tag{1.5}$$

4

This new effective Bain matrix can then be inserted into the compatibility equation to determine if the twin can form a compatible habit plane with the parent austenite.

$$\overline{Q}\,(\lambda Q U_i + (1 - \lambda)U_j) - I = b \otimes \hat{m} \tag{1.6}$$

For nickel titanium there are 192 solutions to the above equation (96 Type I twins and 96 Type II twins) that can create compatible interfaces between austenite and martensite phases. However, it is important to note the limits of this mathematical construction in describing the actual material behavior. The creation of an effective Bain matrix assumes an infinitely refinable mixture of the compatible martensite variants as one gets close to the martensite/austenite interface. In reality, there is a finite limit to the sizes of these twin laths, as well as an energy penalty to be paid for the increases in interfacial area, which limits the accuracy of this approach. However, strict compatibility is not required at the austenite/martensite interface and an elastic zone at the boundary can alleviate a small mismatch in the phase compatibility. This means that, despite their name, the Habit Plane Variants do not form a true habit plane and have some thickness to their interface.

<center>SECTION 1.3: TRANSFORMATION IN SINGLE CRYSTALS</center>

Transformation strain and habit plane selection in nickel titanium single crystals have been examined through experiments which validate the phenomenological model of martensite formation for simple loading conditions and arbitrary crystallographic orientations [30,33–37]. Under tensile loading, it was found that the calculated martensite transformation strain differed from the saturated Lüders-like strain but matched well with strains that were fully recoverable via the shape memory effect. This discrepancy between the Lüders and recoverable strain is consistent with either an incomplete transformation at the end of the transformation plateau that completes at higher stresses, or with detwinning of alternate martensite variants at those same higher stresses. In either case, single

crystal data is consistent with the notion of a single Habit Plane Variant (HPV) completely replacing the parent austenite volume in a single crystal at the 'end' of transformation as predicted by phenomenological models. Additionally, specific habit planes can be identified in single crystal samples when they are placed in tension. This allows for the identification of the HPVs that dominated the transformation. [30,31,33] Measured plane traces match well with predictions based on the Schmid factor of each variant. Under the minimally constrained conditions of a single crystal it was shown that the total strain accommodated by martensite and the particular martensite variant formed could be predicted for an arbitrary crystal orientation in simple tension. [33]

Characterization of single crystals under compression [34,35,38] have also been performed. However, due to the non-local transformation of bulk NiTi under compression, no defined habit plane is formed, which makes macroscopic identification of the particular active HPVs extremely difficult. Rather, these studies [34,35,38] focused on the critical resolved shear stress required for transformation and the relative activity of plastic slip compared to martensite transformation. In both respects, phenomenological predictions of recoverable strain agreed with experimental results for orientations where the relative Schmid factor of martensite transformation was much higher than that for plastic slip [34,35,38]. While the interaction between bulk plasticity and martensite transformation make the results more ambiguous than in the simple tension case, these compression studies provide confirmation of phenomenological theory under simple loading conditions. More recently, single crystal-like experiments [36,39–42] were performed on micropillars in compression. At the microscale, bulk plasticity was suppressed in solutionized samples [36] and individual CVPs formed with distinct habit planes Under these largely unconstrained conditions, reasonable agreement between experiment and phenomenological predictions of dominant transformation variants under compressive loads was found.

Various experiments and models [43–48] have extended the insights of single crystal data to polycrystalline NiTi, where additional intergranular constraints complicate the local stress state in

individual grains. For example, one application considers a polycrystal to be an averaged collection of single crystals, with orientations determined by the orientation distribution function (ODF) of the polycrystal population. An estimate of the total recoverable strain for either shape memory [45] or superelasticity [44,49] can then be made by assuming complete transformation to martensite in each grain and averaging their independent contributions. By ignoring complications of the local stress state and other constraints, and choosing the most favorable single variant of martensite, this averaging produces an upper bound that overestimates the behavior of polycrystalline samples by almost 100% of the measured strain in a textured polycrystal. [44,49] However, the approach does capture the trends of maximum accommodated strains in textured, rolled material along various loading axes between rolling and transverse directions. Another estimation can be made by considering the most favorable HPV—rather than the individual variant—of martensite. [44] While this calculation better matches the recovered strain magnitude, it loses orientation dependence when compared to experimental data and also overestimates the accommodated strain by ignoring intergranular constraints. Another option is to consider the Taylor bound of accommodated strains for single crystals, in which multiple HPVs of martensite are allowable. [44,46,48,50] This consideration includes the compatibility requirements of intergranular interaction and most closely matches experimental strain levels. However, it does not extend to match the orientation dependence of strain, and in underestimates the recoverable strains of polycrystalline specimens with certain crystallographic textures.

SECTION 1.4: POLYCRYSTALS AND SUBGRAIN-LEVEL TRANSFORMATION

Experimental analysis of microstructural transformation in polycrystalline NiTi is more difficult than that for single crystals. *In situ* TEM and synchrotron XRD studies [25,27] have resolved subgranular local strain and crystal structure in polycrystalline superelastic NiTi specimens. These measurements provide detailed quantitative information relating deformation to microstructure, but were limited to measuring the deviatoric lattice strains in the austenite phase

and inferring martensite transformation in those areas where the austenite diffraction pattern could not be resolved. Linking full field strains for both austenite and martensite phases to underlying microstructural features—an extension of diffraction-based studies—is the purpose of adopting the SEM-DIC method described in the Chapter 2.

Additional measures of intergranular constraint have been observed qualitatively using a various experimental methods. In bulk polycrystals, both optical [22] and EBSD [17] based techniques have documented heterogeneous transformation of subgrain regions of coarse grain nickel titanium. In both cases, the transformation progressed in a self-catalytic fashion, with individual martensite laths nucleating new transformation across grain boundaries. These experiments provide insight into where and in what configuration martensite transformation takes place in a polycrystal, but provide little information on how this transformation accommodates strain within and across microstructural features.

Many models [51–55] have been proposed to tackle the problem of predicting transformation in polycrystalline material despite a lack of quantitative empirical data. Many modify the extent of martensite transformation based on constraints of surrounding grains or additional competing deformation modes. The best validation available for these models has been either macroscale stress-strain data or mesoscale strain fields. While these data validate the averaged results of these models, the details of their assumptions are untested. The experimental methodology used in this research was developed to generate the highly spatially resolved experimental data and analyses required to either verify the assumptions of current models, or to provide the information necessary for the development of a more comprehensive model.

SECTION 1.5: THE STRAIN MEMORY EFFECT AND FUNCTIONAL FATIGUE OF SUPERELASTIC SMAS

Under displacement-controlled cyclic loading, superelastic compositions of nickel titanium exhibit functional fatigue [14,36,53,56–61]. Functional fatigue is defined by a shift in the characteristic strains and stresses associated with martensitic transformation and recovery during cycling, as shown in Figure 1. In superelastic material, the stress required to nucleate a macroscopic martensite band tends to decrease with cycling, along with the total recovered transformation strain, resulting in a reduction in total hysteresis over each subsequent cycle. Macroscopically, superelastic samples accumulate residual strain under cycling, which is a mixture of locked-in martensite and plasticity [53,59,61]. The macroscopic changes that occur after cycling a specimen from austenite to martensite and back can also be observed during incomplete cycling of the material, for example during the pulsile loading of SMA cardiac stents [3,57,62,63]. Each section of the macroscopic stress-strain response is independently affected by loading history, indicating that local history impacts later martensite transformation. If these history effects were a global phenomenon, partial transformation cycles would affect the entire stress-strain response rather than producing segment-by-segment drops in the nucleation and propagation stress observed over previously traversed macroscopic strains. This piecewise sensitivity to loading history is indicative of structural changes taking place in areas of the SMA after each portion independently transforms between austenite and martensite. The details of this structural change, whether it is related to a change in how the martensite forms or due to residual damage associated with martensite transformation, is the subject of much previous research.

Recent experimental and computational work indicates that plasticity occurs concurrently with martensitic transformation, rather than as a subsequent process at the end of the macroscopic stress plateau. Neutron diffraction studies have been used to differentiate elastic, transformation,

and plastic strains in polycrystalline specimens. In the early stages of loading, elastic strain in the austenite phase stabilizes at approximately 0.0025 axial strain prior to the start of martensitic transformation [64]. However, as loading continues, plastic deformation plays an active role prior to the saturation of initial macroscopic martensitic transformation Measurements indicate that rehardening starts in superelastic tension when the sample reaches nominally 75% of the strain necessary to macroscopically exhaust the initial transformation to martensite in the specimen. Additionally, a recent micromechanical model of superelastic transformation in a generalized 2-D shape memory alloy includes plasticity as a possible deformation mechanism and demonstrates how the simultaneous activity of slip systems can bridge incompatibilities between regions of martensitic transformation in a polycrystalline shape memory alloy [53].

One of the difficulties in considering plasticity occurring concurrently with martensitic transformation is that compatibility between the austenite and martensite variants affects the development of dislocation networks, and thus the character of functional fatigue. The intensification of dislocation networks across superelastic cycles in a typical superelastic alloy, where there is no compatibility between the austenite and lattice correspondence variants of martensite, is a possible explanation of the strain memory effect [6,14] and return point memory [12,65,66]. Here, the strain memory effect refers to a return to the mesoscale/microscale transformation configuration with cycling, and return point memory refers to the similarity in macroscopic stress-strain curves with incomplete cycling. These effects are the meso- and macroscopic consequences, respectively, of the repeated transformation of austenite to a particular set of martensite variants at the microstructural length scale. This set of variants is stabilized or 'blueprinted' by persistent dislocation networks formed at the boundaries of martensite laths during the first superelastic cycle. [14,36]

10

In materials without austenite-martensite compatibility, dislocation networks that form during initial martensitic transformation have been observed to persist for multiple superelastic cycles. Using *in situ* mechanical testing in a transmission electron microscope, superelastic test coupons that were macroscopically transformed into martensite showed extensive dislocation networks in their unloaded state [36,57,67,68]. The importance of martensitic transformation towards the formation of dislocation networks was further highlighted by combined experiments and modeling of superelastic single crystal micropillars, in which dislocation loops formed as the austenite was 'pinched' between two martensite variants constituting a growing twin. Drawn out dislocation loops appeared solely where martensite twins formed, based on the boundary of the looped and dislocation-free austenite pillar [36,68,69]. These findings indicate that dislocation structures can cross the austenite-martensite phase boundary during cyclic loading, and that these mobile dislocations accumulate with each loading cycle. Similarly, pulsile fatigue experiments of superelastic material produced bands of plastically deformed austenite, and areas of retained martensite that exhibited lower dislocation density as determined by TEM [57]. Dislocations formed at the martensite-austenite interface and in the wake of martensite recovery, but appeared to be located principally in the austenite phase. These dislocation networks are intimately related to martensite/austenite compatibility, as they are unobserved in alloys where the two phases maintain coherent boundaries. In materials where compatibility exists between the austenite phase and each individual martensite variant (referred to as $\lambda_2 = 1$ alloys, in reference to the middle eigenvalue of their martensite Bain matrices), both the accumulation of residual plastic strain and the persistence of martensite structures with cycling are small [70].

As previously discussed with the micropillar experiments, the compatibility conditions between martensite and austenite during transformation lead to the close association of

dislocations with martensite-austenite interfaces. Though the interface between twinned martensite and austenite is commonly referred to as a habit plane, implying compatibility between the two phases, the crystallographic compatibility of the B2 to B19′ transformation is not perfect for near equiatomic nickel titanium [33,71–73], as described earlier. Refinement of the twinned martensite laths and a zone of elastically deformed material is needed to maintain compatibility across the atomically sharp austenite-martensite interface. The component correspondence variants (CVs) that are paired to create a habit plane variant (HPV) are not individually compatible with the austenite and cannot be accommodated with an elastic boundary layer. Modeling work [69] has explained the formation of residual dislocation loops in the micropillar experiments, and attributes their formation to the addition of a compatibility stress at the martensite/austenite interface to the global applied stress. Other alloys have been found that exhibit perfect compatibility between the austenite and martensite phases, where this additional elastic zone does not exist and dislocation networks do not appear to form [70,74–76]. When thermally cycled, these materials exhibited no strain memory during the shape memory process; different martensite variants formed in different patterns each time the material transformed from austenite to martensite. While not definitive—especially for superelastic material—the lack of strain memory in fully compatible alloys strongly suggests that dislocation networks resulting from martensite-austenite incompatibility have a critical role in the secondary formation of martensite in cyclic applications. Without the presence of a dislocation network arising from incompatible correspondence variants to provide a stable blueprint to guide martensitic transformation, the pattern of martensite variants operating in subsequent cycles becomes random [70]. Direct evidence of the coordination between correspondence variants, residual strain, and strain memory has up to now not been shown in alloys that exhibit strain memory behavior.

SECTION 1.6: SUMMARY AND DISSERTATION OUTLINE

Shape memory alloys (SMAs) have been used in a wide range of advanced applications, but the influence of microstructure on local phase transformation in these polycrystalline materials is not well understood. Models of deformation behavior have been based on assumptions about microscale transformation in an attempt to fit observed macroscopic behavior. However, there is a lack of experimental evidence of microscale behavior to validate these assumptions. While research at the microscale has provided insight into the structure and mechanisms of martensite formation, there is no equally detailed *in situ* work that provides a quantitative understanding of the mechanisms and microstructure dependences of transformation in polycrystalline SMAs. The goal of this research is to determine the critical factors that influence the progression of martensitic transformation of superelastic a polycrystalline nickel titanium alloy. To this end, this research seeks to:

1. Determine the validity of using intrinsic grain properties as predictors of the extent of martensitic transformation throughout a polycrystal.

2. Determine which, if any, microstructural features can be used to predict features of martensite transformation in polycrystals.

3. Show how the local influences on transformation compound with mechanical cycling. Specifically, how damage and residual strain accumulate throughout the microstructure and how those residual elements relate to the strain memory effect.

Achieving these goals required the creation of some novel experimental techniques. Digital Image Correlation was adapted to Scanning Electron Microscopy by using some custom distortion

13

correction algorithms. The resulting sub-micron resolution strain fields were able to resolve the martensite transformation in extremely fine detail. When overlaid with the crystallographic data available from Electron Backscatter Diffraction, individual martensite laths could be identified within certain individual grains. Post processing of the same strain fields with a martensite matching algorithm allowed for identification of the transformed martensite variants even in cases where clear martensite laths were not identifiable. The details of the experimental procedures which generated this data can be found in Chapter 2, while the observations of martensite variant formation can be found in the first half of Chapter 3.

The high resolution strain fields captured by SEM-DIC allowed for a large number of measurements to be made in each grain of several polycrystalline specimens. That provided a statistically significant sampling of orientation space to analyze the validity of the phenomenological approach to modeling transformation in superelastic material. Chapter 3 compares the full distributions of strains in grains of similar orientation, showing that the phenomenological assumptions of texture based models are not widely applicable to polycrystalline structures. This is in line with the shortcomings of these models in the literature. Additionally, regression analysis of all the data can be found in Chapter 3 which shows how the resolved stress on twinned martensite structures can have a profound impact on which variants of martensite form during superelastic transformation.

Chapter 4 addresses the accumulation of residual strain in polycrystalline nickel titanium during superelastic fatigue. This addresses objective number 3 for this dissertation research. SEM-DIC allows for all points in the area of interest to be related back to a single reference condition, and so all residual deformation can be tracked through the martensitic transformation of any given cycle. It is shown that the residual strain accumulated at any given point in the polycrystal is highly

dependent on the initial configuration of martensite that transforms there during the first super elastic cycle. The residual strain network left behind is the potential blueprint for the strain memory effect, biasing later martensite transformation to follow the initial transformation configuration.

While this dissertation does accomplish all of the research goals outlined here, there are still several open questions which remain to be addressed. Some are raised by the assumptions used in the analysis presented in this dissertation, while others are simply points of clarification in need of additional research tools. Chapter 5 provides a review of the major findings of this dissertation and suggests future work to address the outstanding questions that arose during the research.
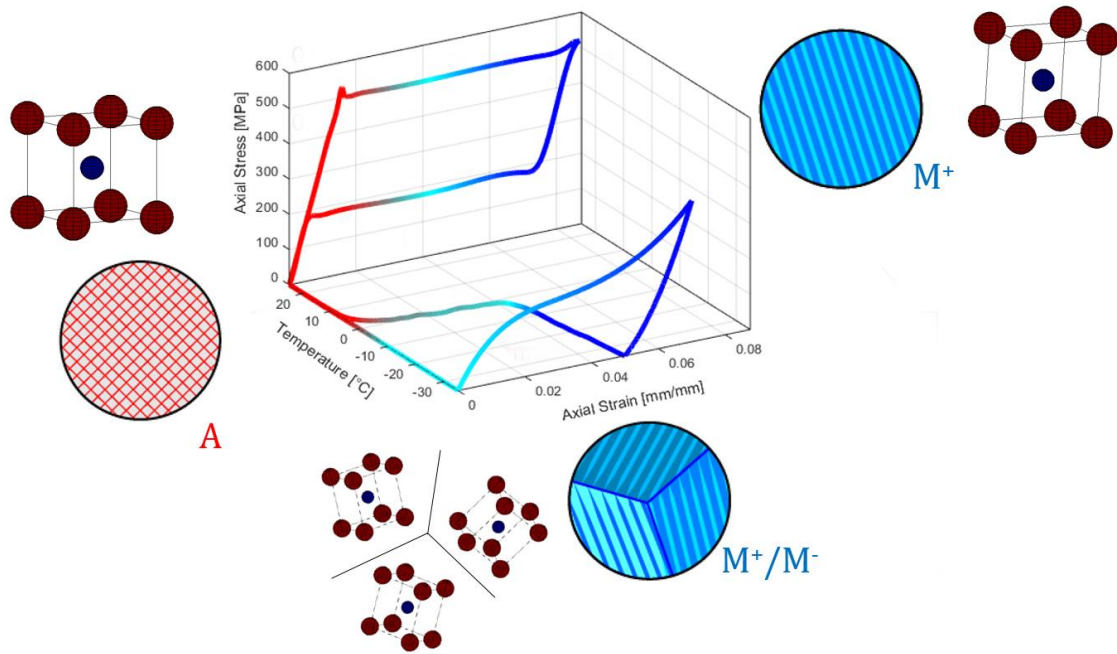
Figure 1.1: Schematic representation of the shape memory and superelastic effects in stress-strain-temperature space. The shape memory cycle is the lower loop involving a temperature transition. The material starts shape set as austenite (red) at a high temperature. The material is cooled and a self-accommodated configuration of martensite (light blue) forms, preserving the parent shape. Deforming this martensite appears plastic, however since it only involves the reorientation of martensite variants (dark blue), the strain can be recovered by heating the sample up to transform back to austenite. The super elastic curve at the top takes place at a temperature above the austenite finish temperature. Here the favorably oriented martensite (dark blue) is stress induced and recovered when load is removed.
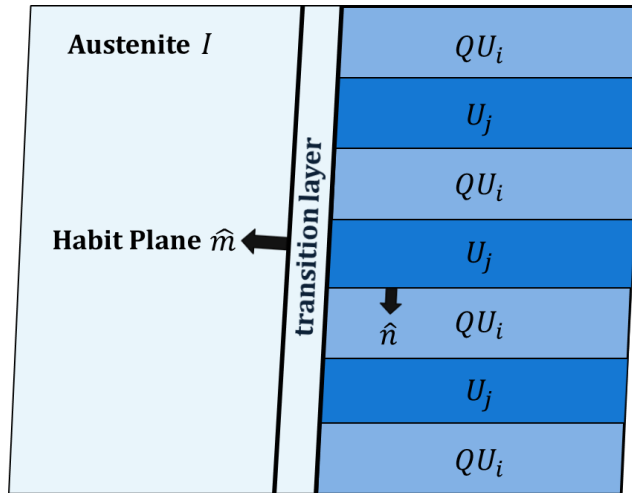
Figure 1.2: Schematic representation of 2 twin-related orientations of martensite forming a habit plane with the parent austenite phase.
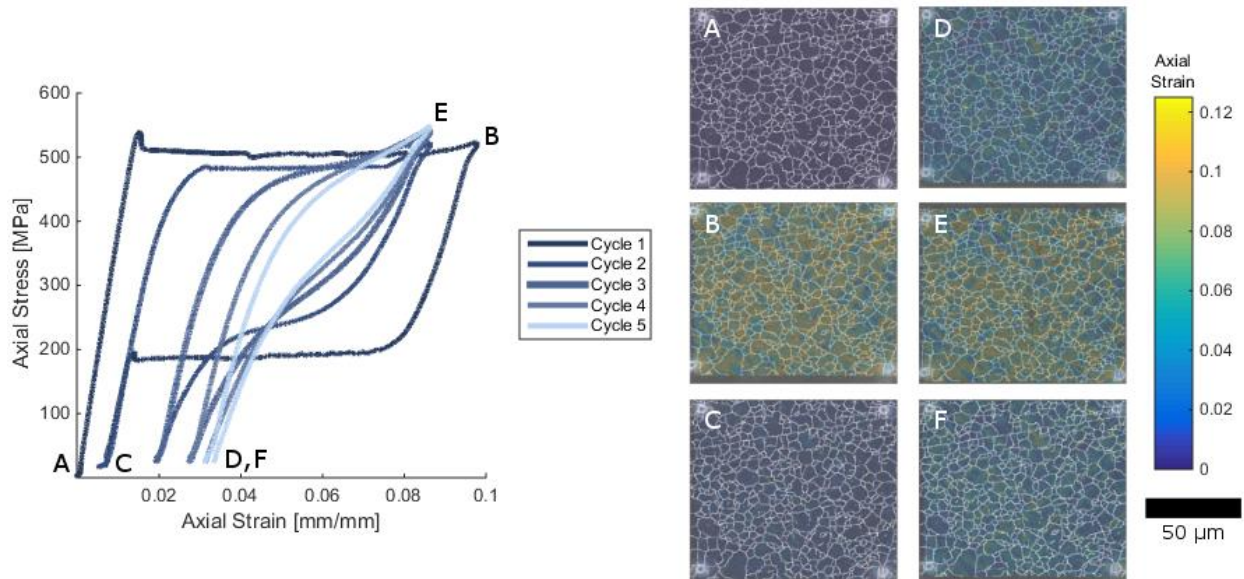
Figure 1.3: Example of functional fatigue and local strain memory in a polycrystalline microstructure. The stress strain curve on the left is real data taken from an in situ experiment and demonstrates the narrowing of the superelastic hysteresis loop during superelastic cycling. The images on the right are the local strain fields taken at the indicated points along the stress strain curve. Notice especially the residual strain accumulation between images A and D as well as the similarity in the strain fields between B and E. The first comparison demonstrates a high degree of heterogeneous strain ratcheting in the sample while the second represents a high degree of microstructural strain memory. Both of these phenomenon will be discussed in detail in Chapter 4.

CHAPTER 2: METHODS AND MATERIALS

This chapter provides an overview of the experimental methods used gather and process the full field strain maps and crystallographic information vital to this dissertation work. Special attention will be paid to the preparation of superelastic specimens, their heat treatment, and the use of nanoscale patterning for distortion-corrected Digital Image Correlation inside of a SEM. Digital Image Correlation itself will also be briefly reviewed, including the special considerations used to apply the technique to Scanning Electron Micrographs. The final section of this chapter describes the method that was developed and employed to make possible the use of crystallographic and full field strain data from multi-cycle superelastic tests to identify the configurations of transforming martensite.

SECTION 2.1: PREPARATION OF NICKEL TITANIUM SPECIMENS

Dogbone-shaped specimens were cut to the dimensions shown in Figure 2.1a with Electro Discharge Machining from 0.480 mm thick superelastic NiTi (50.8 at% Ni) received from Nitinol Devices and Components. The specimen tensile axes were oriented parallel, perpendicular, and at 45° to the sheet rolling direction. Specimens with nominal gage dimensions of 2 mm x 10 mm were heat treated at 625°C for 10 minutes followed by a water quench, resulting in a mean grain diameter of ~4μm (Fig 2.1bc). Specimens were then aged at 450 °C for 10 minutes to achieve superelastic behavior at room temperature[77,78].

TEM analysis was not performed on the aged specimens, however the structure of coarse-grained, aged nickel titanium has been previously characterized in literature. When aged between 400°C to 500°C metastable lenticular Ti_3Ni_4 precipitates form. [79–85] The precipitates preferentially form one of eight variants along one of the four B2 {111} planes in the parent austenite and are semi-coherent below a critical diameter between 150-200 nm. Under stress-free aging conditions, as used here, no orientation preference between the {111} planes occurs, though the precipitates can be biased to form long B2 channels by applying a stress during aging. [79,81] The primary effect of these precipitates is to raise the yield strength of the material. Secondarily, these precipitates also tune the nickel content of the matrix such that it is superelastic at room temperature. [83,84] The lattice mismatch eigenstrains [82,84,85] between the Ti_3Ni_4 precipitates and bulk B2 structure are

$$\varepsilon^{Ti_3Ni_4} = \begin{bmatrix} -0.00417 & 0 & 0 \\ 0 & -0.00417 & 0 \\ 0 & 0 & -0.0257 \end{bmatrix} \tag{2.1}$$

The mismatch in strains will promote the transformation of R-phase, an intermediate phase in the B2 to B19′ transformation, along the broad side of these precipitates, though the B19′ is still favored at the precipitate edges and in the bulk. [81]

The precipitates are not detectable in the SEM-DIC calculated strain fields and do not affect martensitic transformation in the material. They will not be closely considered in this dissertation work. With the minimal time peak-aging treatment used, the thickness dimension of the lenticular precipitates is below the resolution of the DIC images (15 nm/pixel). Based on TEM micrographs of peak aged precipitates, the other dimension of the precipitates are also likely below the smallest subset size (9 by 9 pixels or 1.35 by 1.35 µm) used to calculate strain making any localization from the precipitate structures undetectable at the length scales under investigation. Additionally, longer

over aging treatments (over 15 hours at 500 °C) produce a volume fraction of 0.07 Ti$_3$Ni$_4$ [79] which, using the Johnson-Mehl-Avrami equation

$$f(t) = 1 - \exp(-\left(\frac{t}{\tau}\right)^m)\tag{2.2}$$

where m = 2 for the disc shaped precipitates, would correspond to a 0.0013 fraction at 120 minutes of aging at 500 °C. The 2 hour treatment at 500 °C is roughly equivalent to the 10 minutes at 450 °C used for this aging based on comprehensive austenite finish temperature measurements made elsewhere. [86] Thus, nearly 99.9 % of the material in the heat-treated specimens was still transformable austenite, making its behavior indistinguishable from solutionized NiTi. Finally, the random orientation of these stress-free precipitates made the biasing of martensite transformation due to aligned precipitates [79,81] unlikely compared to the biasing due to the applied stress. So long as the precipitate structure is formed under zero load, and lowers the transformation stress below the yield stress by a sufficient margin to ensure superelastic transformation is the dominant deformation mode, the precipitate structure can safely be ignored for this level of analysis.

Heat treated specimens were mechanically ground and polished to a mirror finish, and their microstructure was characterized by Electron Backscatter Diffraction (EBSD) to determine grain size and crystallographic orientation within a nominal 100 x 100μm area. Platinum fiducial markers were laid down on the specimen surface prior to EBSD scanning to aid in later alignment of the DIC strain field and the crystal orientation field obtained from EBSD. Care was taken to account and correct for any projective distortion from the high imaging angles required for EBSD capture before aligning it with the EBSD grid.

Samples were then patterned for digital image correlation using a self-assembly of gold nanoparticles on a silane surface treatment [52] as seen in Figure 2.1d. The smallest feature produced by the nanoparticle patterning technique was approximately ~50 nm, enabling an image

resolution of 15 nm/pixel. With the nominal sub-pixel resolution of DIC (approximately 0.02 pixel), measuring displacements of 0.3 nm is possible with this pattern.

All *in situ* tests were performed using the Kammrath and Weiss tensile stage shown in Figure 2.2. A nominal strain rate of 10^{-4} s^{-1} was maintained using a constant displacement rate for all specimens. This quasi-static strain rate ensured minimal heat effects for all tests. Load was captured with a 1 kN load cell and with displacement control provided by an LVDT sensor with a resolution of 1 μm. Strain was measured using both the macroscopic displacement and SEM-DIC in post processing.

SECTION 2.2: SCANNING ELECTRON MICROSCOPY AND DIGITAL IMAGE CORRELATION

To capture full-field strains at the microstructural length scale with sufficient spatial resolution to relate them to microstructural features, a methodology combining Scanning Electron Microscopy and distortion-corrected Digital Image Correlation (SEM-DIC) was used following [87–90]. Using this technique, with the appropriate distortion correction and data analysis suite, it was possible to measure the subgranular transformation of austenite to martensite variants in superelastic nickel titanium specimens over relatively large fields of view. The basics of Digital Image Correlation (DIC) and the adaptations needed to attain the necessary level of precision and resolution for this research is described in the paragraphs below.

DIC is a non-contact optical technique used to determine full-field displacements on the surface of a sample with sub-pixel resolution, where grey-scale images of the surface are compared to track the movement of material subsets. [91,92] Subset comparison is done by minimizing a 2-D cross-correlation coefficient with the form:

$$S(x, y, x^*, y^*) = 1 - \frac{\sum F(x,y) \cdot G(x^*,y^*)}{\sqrt{\sum F(x,y)^2 \cdot \sum G(x^*,y^*)^2}} \tag{2.3}$$

where $F(x, y)$ and $G(x^*, y^*)$ are the grey scale values of the pixels at the reference point (x, y) and the deformed point (x^*, y^*), respectively. The local displacement can then be calculated by taking the differences of the best match locations such that

$$u(x, y) = x - x^* \tag{2.4}$$

$$v(x, y) = y - y^* \tag{2.5}$$

Subpixel resolution of (x^*, y^*) can be achieved by using bicubic spline interpolation of the whole pixel values of $G(x^*, y^*)$ to increase the precision of the DIC matching algorithms. In this work, the initial correlation of all captured images was performed using commercial software from Correlated Solutions which has sub pixel registration built into its search algorithm.

One of the biggest strengths of DIC is that it is length-scale independent. DIC was initially developed for use with traditional optical imaging, and extensive work has been performed to remove the spatial distortions of optical elements. Many of these corrections are built into commercial software packages. However, when applying DIC to scanning electron micrographs, far more complex distortions are caused by the rastering and time dependent nature of SEM image capture, the complicated 'shape' of electron focusing lenses, and other factors. Custom MATLAB scripts were created to remove the spatial and temporal distortions from the micrographs used in this work [87,89,93]. This correction process enables SEM-DIC to reach sub-pixel resolution on the order of that achieved in traditional optical DIC systems. With additional optimization of beam intensity and dwell time, two parameters unavailable to optical systems, SEM-DIC can sometimes achieve greater accuracy that optical DIC systems. [87]

The full-field displacement maps can be used to determine surface strains by a local application of continuum strain definitions. These strain calculations were performed using MATLAB scripts, after correcting each initial correlation for SEM distortions. At each point, strain

was calculated by measuring the gradient of a bicubic surface fit of the local neighborhood displacements. This allowed for a tight fit to any discontinuity in the data, such as a sharp habit plane between high and low strain regions, while also limiting the influence of single points of noise that would overwhelm shape function approaches to calculate strain. All measurements were made with regard to the reference configuration to eliminate the need to deform the EBSD data and to keep all calculations in reference to the parent austenite.

SECTION 2.3: DETERMINING MARTENSITE TRANSFORMATION CONFIGURATION

A limitation of the strain-based analysis of materials is the inability to attribute strain to specific deformation mechanisms without additional information at each measurement point. One option to determine which deformation system is active involves finding traces of localized strain and relating them to the analytically-derived traces of crystallographic planes for possible transformation variants or slip systems [24,87]. This process is limited to identifying isolated martensite laths or clearly defined slip traces in austenite. An improved approach was therefore developed that determines which of the possible martensite configurations have formed at every point, rather than only those that form near a clearly delineated mesoscopic austenite-martensite interface. Here, the configuration of habit plane variants and correspondence variants that most closely matches the measured surface strain is calculated on a point-by-point basis across large fields of view. The procedure to achieve this is described below.

Experimentally measured strains were correlated to theoretically calculated transformation strains by first calculating the transformation strains of all possible correspondence variants (CVs) and habit plane variants (HPVs). To accomplish this, the Bain Transformation Matrices (U_i) were calculated for each of the 12 martensite CVs possible from the undeformed austenite configuration based on the known lattice parameters for the martensite phase [1,29–32]. For nickel titanium,

23

these have the form of $R^T U_1 R$ where R is a member of the cubic symmetry group $\mathcal{L}_{cubic}$ and U_1 has the form:

$$U_1 = \begin{bmatrix} \gamma & \epsilon & \epsilon \\ \epsilon & \alpha & \delta \\ \epsilon & \delta & \alpha \end{bmatrix} \tag{2.6}$$

The following parameters were used: $\gamma = 0.9563$, $\epsilon = -0.0427$, $\alpha = 1.0243$, and $\delta = 0.058$ [31]. From the Bain stretch matrices, transformation strains for each of the correspondence variants were determined from continuum mechanics. To simplify the analysis and have the proper work conjugate to the experimentally measured engineering stresses, the Biot strain was used. The Biot (ε_{Biot}) strain is defined as

$$\varepsilon_{Biot} = U - I \tag{2.7}$$

where I is the identity matrix.

After calculating the (Biot) transformation strains (ε_{CV}^i) and Bain matrices for the 12 correspondence variants, the next step was to construct effective Bain matrices for each of the 192 HPVs (please see [1,31,94,95] or Chapter 1 for details on this procedure), as well as the relative fractions of CVs in each HPV. The effective Bain matrix of an HPV is a linear combination of the Bain stretch matrices of its CV components, and represents the mean stretch that results from austenite transforming to the HPV combination. From the relative volume fractions of each CV in the HPV (ϑ and $1 - \vartheta$), the Biot strain for each HPV in the reference configuration was given by:

$$\vartheta \varepsilon_{CV}^{n1} + (1 - \vartheta) \varepsilon_{CV}^{n2} = \varepsilon_{HPV}^n \tag{2.8}$$

Note that the Biot strain is assumed to be linear with the Bain stretch matrix, which allows for this equality to hold. The compatibility of each HPV with all other HPVs was then determined from the calculated strain of each HPV by a zero-sum shear definition [94]. HPV pairs, ε^{HPV1} and ε^{HPV2}, whose sum resulted in purely dilatational strain were defined as compatible, i.e.

$$\epsilon_{ijk}\epsilon_{pqr}\left(\varepsilon_{jq}^{HPV1} - \varepsilon_{jq}^{HPV2}\right) = 0 \qquad (2.9)$$

where ϵ_{ijk} is the permutation tensor. Other definitions of compatibility, such as the formal calculation of habit planes for each HPV pair, can also be used to limit the potential solution set. The relatively large set of compatible variants generated by the compatibility condition of Equation 2.7 was chosen to allow for the maximum possible combinations of compatible HPVs (1650 for the 96 Type II HPVs) and to allow for small incompatibility strains between phases compared to the perfect match required by the aforementioned habit plane calculations. However, note that the larger set of solutions implied by the definition of compatibility may overestimate the ability of HPVs to coexist. Independent of the compatibility definition used here, it was necessary to allow for multiple HPVs to exist at a given point because of the 'smeared' nature of DIC strain calculation. Local strain can be effectively mixed with the immediate surroundings of an individual point, and thus a similar mixing was required in the phase fitting process.

In order to match the experimental data to the calculated strain values, the reference strains for each CV and HPV were rotated into the same orientation as the grain under investigation. Using the Euler Angles collected from EBSD and aligned with the DIC strain field, a rotation matrix ($\boldsymbol{R}$) was constructed to transform matrices from the reference to the grain orientation in X-Y-Z Cartesian image space of the DIC strain fields. Note that the inverse procedure cannot be accomplished due to the inability to experimentally measure out-of-plane strains. All the rotated strain values were stored in the new local configuration:

$$\boldsymbol{\varepsilon'} = \boldsymbol{R\varepsilon R}^T \qquad (2.10)$$

For each grain, a 'strain space' representation, $\tilde{\boldsymbol{\varepsilon}}$, of each HPV and CV was created based on its rotated (ε'_{xx}, ε'_{yy}, ε'_{xy}) strain values. These points will later be compared against experimental data to determine the most probable HPV and CV transformation combination.

25

Each measured displacement (strain) data point in a grain was independently matched to the HPV and CV solution cloud. The ith strain point ($\tilde{\boldsymbol{\varepsilon}}^i$) was placed in the same strain space as all of the rotated HPV and CV representations ($\tilde{\boldsymbol{\varepsilon}}^n_{HPV}$ and $\tilde{\boldsymbol{\varepsilon}}^m_{CV}$), and then compared to all possible HPV and CV solutions. The mathematical constructions used to compare each test point to possible solutions were based on a distance minimization in the constructed strain space of each grain (Figure 3). In the case of two-phase mixtures (e.g. austenite with HPV) the distance from the test point to the line segment connecting the points for each phase in strain space was minimized. Similarly, for three-phase mixtures (e.g. austenite with two compatible HPVs) the distance minimization was performed between the test point and the triangular plane face connecting the three phase points. The phase fraction in either case was calculated using lever law-like rules to find the combination that resulted in the lowest root mean squared error mixture to represent each strain point. These constructions are represented graphically in Figure 3 and mathematically below.

The single HPV plus austenite solution was tested first. The minimum root mean squared error ($\Delta\varepsilon_{RMS}$) from the ith strain point ($\tilde{\boldsymbol{\varepsilon}}^i$) to a phase fraction ($\lambda_{HPV} \in (0,1]$) of the nth HPV ($\tilde{\boldsymbol{\varepsilon}}^n_{HPV}$) was determined according to:

$$\Delta\varepsilon_{RMS} = \frac{|\lambda^n_{HPV}\tilde{\varepsilon}^n_{HPV} - \tilde{\varepsilon}^i|}{\sqrt{3}} \tag{2.11}$$

$$\lambda^n_{HPV} = \frac{\tilde{\varepsilon}^n_{HPV} \cdot \tilde{\varepsilon}^i}{|\tilde{\varepsilon}^n_{HPV}|^2} \tag{2.12}$$

The $\Delta\varepsilon_{RMS}$ value was taken as the baseline error for the associated strain point, where any other solution had to provide a lower error to be considered as a potential match. After exhausting the single variant solutions, a similar process was then used to determine the minimum RMS error for

any pair of compatible HPVs (e.g., $\tilde{\boldsymbol{\varepsilon}}^n_{HPV}$ and $\tilde{\boldsymbol{\varepsilon}}^m_{HPV}$ that satisfy the conditions of Equation 2.9) of any phase fraction combination

$$\lambda^n_{HPV}, \lambda^m_{HPV} \in (0,1) \tag{2.13}$$

$$\lambda^n_{HPV} + \lambda^m_{HPV} \leq 1 \tag{2.14}$$

as follows:

$$\Delta\varepsilon_{RMS} = \frac{|\lambda^n_{HPV}\tilde{\varepsilon}^n_{HPV} + \lambda^m_{HPV}\tilde{\varepsilon}^m_{HPV} - \tilde{\varepsilon}^i|}{\sqrt{3}} \tag{2.15}$$

$$\tilde{\boldsymbol{\varepsilon}}^i_{in\,plane} = \tilde{\boldsymbol{\varepsilon}}^i - \left(\tilde{\boldsymbol{\varepsilon}}^i \cdot \frac{(\tilde{\varepsilon}^n_{HPV} \times \tilde{\varepsilon}^m_{HPV})}{|\tilde{\varepsilon}^n_{HPV} \times \tilde{\varepsilon}^m_{HPV}|}\right)\left(\frac{(\tilde{\varepsilon}^n_{HPV} \times \tilde{\varepsilon}^m_{HPV})}{|\tilde{\varepsilon}^n_{HPV} \times \tilde{\varepsilon}^m_{HPV}|}\right) \tag{2.16}$$

$$\boldsymbol{T} = \begin{bmatrix} \tilde{\varepsilon}^n_{HPV,1} & \tilde{\varepsilon}^m_{HPV,1} \\ \tilde{\varepsilon}^n_{HPV,2} & \tilde{\varepsilon}^m_{HPV,2} \\ \tilde{\varepsilon}^n_{HPV,3} & \tilde{\varepsilon}^m_{HPV,3} \end{bmatrix} \tag{2.17}$$

$$\begin{pmatrix} \lambda^n_{HPV} \\ \lambda^m_{HPV} \end{pmatrix} = \tilde{\boldsymbol{\varepsilon}}^i_{in\,plane}/\boldsymbol{T} \tag{2.18}$$

For points that transformed into more than 50% HPV (as determined by the sum of λ_{HPV} values of any single or multiple HPV-only variant solutions), the possibility of detwinning of the primary HPV ($\tilde{\boldsymbol{\varepsilon}}^n_{HPV}$) into its component CVs ($\tilde{\boldsymbol{\varepsilon}}^{n1}_{CV}$, $\tilde{\boldsymbol{\varepsilon}}^{n2}_{CV}$) was checked. This was performed following the same mathematical framework as in the multiple HPV solution, where $\tilde{\boldsymbol{\varepsilon}}^n_{HPV}$, $\tilde{\boldsymbol{\varepsilon}}^m_{HPV}$, and their respective λ_{HPV} values were replaced with $\tilde{\boldsymbol{\varepsilon}}^{n1}_{CV}$, $\tilde{\boldsymbol{\varepsilon}}^{n2}_{CV}$, and the corresponding λ_{CV}:

$$\Delta\varepsilon_{RMS} = \frac{|\lambda^{n1}_{CV}\tilde{\varepsilon}^{n1}_{CV} + \lambda^{n2}_{CV}\tilde{\varepsilon}^{n2}_{CV} - \tilde{\varepsilon}^i|}{\sqrt{3}} \tag{2.19}$$

$$\tilde{\boldsymbol{\varepsilon}}^i_{in\,plane} = \tilde{\boldsymbol{\varepsilon}}^i - \left(\tilde{\boldsymbol{\varepsilon}}^i \cdot \frac{(\tilde{\varepsilon}^{n1}_{CV} \times \tilde{\varepsilon}^{n2}_{CV})}{|\tilde{\varepsilon}^{n1}_{CV} \times \tilde{\varepsilon}^{n2}_{CV}|}\right)\left(\frac{(\tilde{\varepsilon}^{n1}_{CV} \times \tilde{\varepsilon}^{n2}_{CV})}{|\tilde{\varepsilon}^{n1}_{CV} \times \tilde{\varepsilon}^{n2}_{CV}|}\right) \tag{2.20}$$

$$\boldsymbol{T} = \begin{bmatrix} \tilde{\varepsilon}^{n1}_{CV,1} & \tilde{\varepsilon}^{n2}_{CV,1} \\ \tilde{\varepsilon}^{n1}_{CV,2} & \tilde{\varepsilon}^{n2}_{CV,2} \\ \tilde{\varepsilon}^{n1}_{CV,3} & \tilde{\varepsilon}^{n2}_{CV,3} \end{bmatrix} \tag{2.21}$$

$$\begin{pmatrix} \lambda^{n1}_{CV} \\ \lambda^{n2}_{CV} \end{pmatrix} = \tilde{\boldsymbol{\varepsilon}}^i_{in\,plane}/\boldsymbol{T} \tag{2.22}$$

If the detwinned volume fractions were between zero and one, the twinned (φ_t) and detwinned (φ_{dt}) fractions were calculated based on the volume fraction (ϑ) of CVs in the twin from Eq. 2.2:

$$\varphi_t = \begin{cases} \frac{\lambda_{CV}^{n1}}{\vartheta}, & if \ \frac{\lambda_{CV}^{n1}}{\vartheta} \leq \frac{\lambda_{CV}^{n2}}{1-\vartheta} \\ \frac{\lambda_{CV}^{n2}}{1-\vartheta}, & if \ \frac{\lambda_{CV}^{n1}}{\vartheta} > \frac{\lambda_{CV}^{n2}}{1-\vartheta} \end{cases} \tag{2.23}$$

$$\varphi_{dt} = \begin{cases} \lambda_{CV}^{n2} - \frac{\lambda_{CV}^{n1}}{\vartheta}(1-\vartheta), & if \ \frac{\lambda_{CV}^{n1}}{\vartheta} \leq \frac{\lambda_{CV}^{n2}}{1-\vartheta} \\ \lambda_{CV}^{n1} - \frac{\lambda_{CV}^{n2}}{1-\vartheta}\vartheta, & if \ \frac{\lambda_{CV}^{n1}}{\vartheta} > \frac{\lambda_{CV}^{n2}}{1-\vartheta} \end{cases} \tag{2.24}$$

If the total volume fraction of HPVs in the initial solution was less than 50%, there was therefore no need to calculate λ_{CV}^n, and the following conditions were set:

$$\varphi_t = \sum_n \lambda_{HPV}^n \tag{2.25}$$

$$\varphi_{dt} = 0 \tag{2.26}$$

The configuration with the lowest $\Delta\varepsilon_{RMS}$ was selected as the best fit for each point. All identifiers for the twinned and detwinned structures and their volume fractions were recorded for further analysis, such as correlating transformation fraction to residual strain, which will be discussed in Chapter 4.

It is important to note that considering the HPV combinations in addition to their fundamental CV components may seem redundant, but it is necessary to examine both the enhanced compatibility of HPV structures with the parent austenite and with each other. The above algorithm could be reconfigured to only consider mixtures of CVs, as all the HPV structures would be a subset or special case of the complete CV solution set. The overall fit and error of such a CV-only solution would also be comparable to explicitly including the HPV sub-solutions. However, such a fit would require the use of strict compatibility between three or more CV solutions rather than the looser HPV compatibility conditions used here. This could potentially miss some of the

Gaussian spread inherent to working with DIC strain fields. Also, it would require additional steps to determine the maximum compatibility of a CV mixture with the parent austenite if HPV solutions were not explicitly included at the outset. For these practical reasons, it was determined that redundancy of explicitly including the HPV solutions in the CV solution set was a worthwhile choice as it eliminates extra steps between the martensite fitting and interpretation of results.

A shortcoming of this approach is the lack of a guaranteed unique solution when only in-plane strains are measured, as is this case with surface strain measurement techniques like 2-D DIC. Of the six independent strain components that describe each correspondence variant, habit plane variant, or their combinations, only three could be matched to experimental data. Unique identification of the exact configuration of martensite was therefore not guaranteed, as symmetry related variants can be indistinguishable in three-dimensional strain space and multiple HPVs can occupy identical $\tilde{\boldsymbol{\varepsilon}}_{HPV}$ points. At maximum, four distinct points in 6-D strain space can share the same 3-D in-plane projection. However, there is sufficient information in the 3-D projection to determine the configuration types present in a local mixture. For example, it is possible to determine if a point lies on a line connecting several coincident, but incompatible, HPVs to the origin; when this happens, it is strong evidence that the local strain is a result of a single HPV, though determining which specific HPV may not be possible. Similarly, it is possible to determine when a point lies outside the bounds of all HPV solutions, which requires the presence of detwinned correspondence variants. The relative position outside the HPV bound can also assist in the determination of the direction in and degree to which detwinning progressed, given the sparse distribution of the 12 possible CV solutions compared to the 192 HPVs and the lack of duplicity in the CV solutions. Thus, the best fit determined by this method may be better characterized as a set of non-unique solutions which all fit the experimental data equally well.

However, the properties of the members of the solution set, such as their detwinned and twinned volume fractions, can be defined through strain analysis alone.

For multi-cycle analysis, the solution set of martensite variants can be limited based on transformation history. Using the algorithm alone, there is no preference to repeat the same configuration of martensite in consecutive cycles. The solution with the lowest error will be found independently for each cycle if additional constraints are not applied. This corresponds to the *history-free* assumption that martensite is infinitely reorientable during each transformation cycle and that transformation has no history bias. As previous work [6,12,14,65,66] has shown a strong strain memory effect, where the same martensitic configuration repeatedly transforms and recovers, a strict history dependent addition was made to the code to restrict transformation under cycling. *Strict history* assumption in this case means that after all the possible martensite variants are made available in the first cycle, all subsequent fitting is done with only those variants which appeared in the first cycle's configuration. Each point is restricted independent of its neighbors. This conforms to the observed strain memory behavior on the macro and micro length scales, as it is likely from the high degree of similarity in the strain data for each cycle at max load that martensite transformation is repeating in each cycle. Both the history-free and strict-history conditions are calculated in Chapter 4 to compare the two extremes of history dependence against the experimental data.
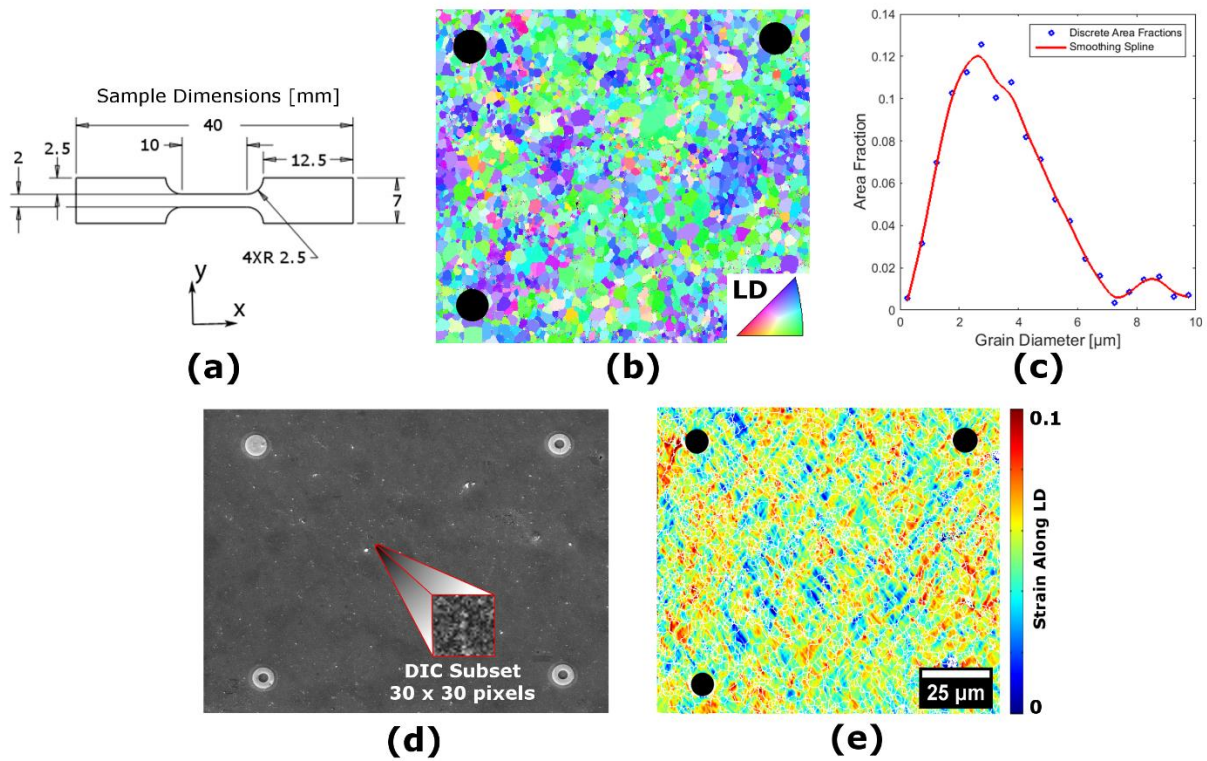
Figure 2.1: (a) Sample dimensions; (b) EBSD scan of the loading direction orientation used to determine grain boundaries and local orientation; (c) area fraction vs. grain diameter; (d) grain boundaries aligned with the nanoparticle DIC pattern; (e) grain boundaries displayed as white lines in the strain field to correlate strain and orientation fields for analysis. The black spots in (b) and (e) are the same platinum markers shown in (d) and are used to align the data sets and delineate a nominal 100 μm square.
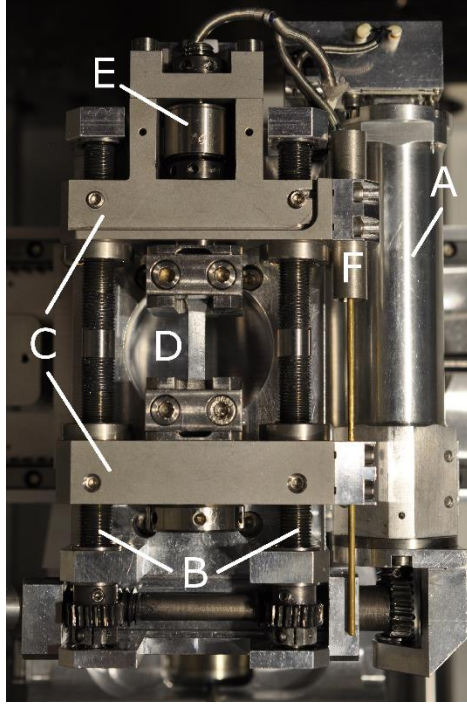
Figure 2.2: Kammrath and Weiss Load Frame used during in situ experiments. Marked items are A: High torque stepper motor, B: Counter-rotating screw drives, C: Equal displacement crossheads to keep the sample centered during testing, D: Dummy sample in grips, E: Interchangeable load cell (1kN capacity used for testing), F: LVDT Linear Encoder for secondary macroscopic strain measurements.
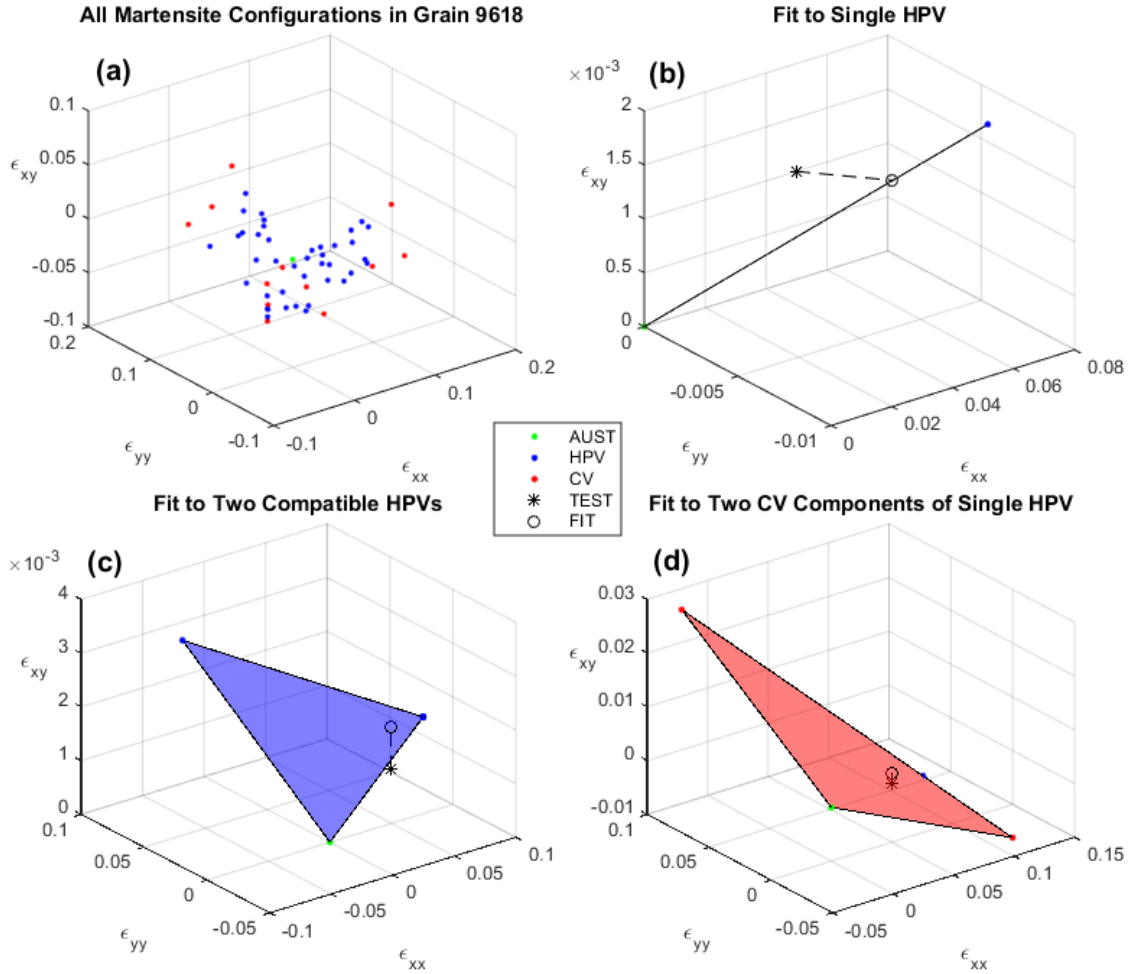
Figure 2.3: (a) Distribution of CV and HPV strain points in the reference frame of Grain #9618. Note that the apparent clustering of HPV and CV solutions is due to the large span of strains included in the figure. (b) A graphical representation of fitting a test point (*) to the best match phase mixture of a single HPV and austenite. Similar representations of (c) fitting the test point to a three phase mixture can be constructed for multiple HPVs and (d) the decomposition of a single HPV into its CV components.

CHAPTER 3: MICROSTRUCTURAL INFLUENCES OF MARTENSITIC TRANSFORMATION

One of the major challenges facing the greater shape memory alloy community is the development of effective modeling tools to predict the transformation behavior of polycrystalline SMAs. Current models make significant assumptions about how transformation progresses through a microstructure. Unfortunately, there is little quantitative experimental data available to examine the assumptions that go into these models. To that end, a large part of this dissertation work was to examine the critical factors controlling martensite transformation and gather empirical evidence to that provides a basis for evaluating the assumptions required in extant models and for future development of new models.

In this chapter the basics of microscale martensite transformation will be presented for two major orientations of rolled nickel titanium sheet. After this qualitative introduction, the extent of martensite transformation will be quantified using the technique outlined in Chapter 2. Using the martensite configuration of these tests, a logarithmic regression is used to determine the factors influencing the final configuration of martensite in fully transformed superelastic material. Lastly, a comparison of local strain distributions is used to examine the common assumption that similarly oriented grains transform similarly.

SECTION 3.1: GENERAL OBSERVATIONS OF MICROSCALE MARTENSITE TRANSFORMATION

To provide an example of the progression of martensite transformation through a polycrystalline sample, SEM-DIC was used here to track the evolution of strain in both austenite and martensite phases. (Figure 3.1) The specimen was oriented with the rolling direction of the

parent sheet parallel to the loading axis. At a globally applied stress of ~525 MPa, a single macroscopic martensite band nucleated near the grips and then propagated though the gage section under a nominally constant stress of 500 MPa. A single martensite front can be seen progressing through the SEM-DIC microscale strain maps in Figures 3.1b. At the microstructural length scale shown in Figure 3.1b, the martensite front was diffuse and formed a crosshatch-like structure in advance of the stable band, where stability is defined as a less than ±0.25% change in local strain value from the previous measurement. This diffuse cross-hatched region extended approximately 150 μm beyond the stable region of the band. The areas that first transformed in the diffuse band as the front progressed tended to attain the highest local strains when transformation in those areas saturated. When a region was subsumed by the stable macroscopic band, strain accumulation in that region ceased and local strain levels remained nominally constant (within the aforementioned ±0.25%) as loading continued and the macroscopic band propagated past the region. Nearly all of the deformation that a microstructural neighborhood could accommodate was accommodated immediately, and any transformation or recovery (within the limits of detection) took place only at the band front rather than within the already transformed martensite band.

By taking a local average of strain values in the region shown in Figure 3.1c, which was fully inside the macroscopic martensite band, it can be determined that 'complete' transformation accommodated an average of 7.5% longitudinal strain. However, this strain was accommodated remarkably heterogeneously. Some sub-grain areas experienced strains of up to 12%, while others essentially remained near 0% strain despite the large amounts of transformation that could encompass their boundary. Comparison of strain and EBSD data indicates that areas accommodating larger strains developed primarily along grain boundaries while the low strain regions generally lay in grain interiors. The lower strains found primarily in grain interiors may be

35

the result of low strains blending with high strain regions due to the finite size of the strain calculation window, which reduces strain contrast around areas with rapidly changing strains.

The progression of martensite transformation in polycrystals is largely of the same form for both transverse and rolling direction loading axes. The pattern of a sparse crosshatch which backfills at the completion of transformation is the rule for both specimen orientations. Therefore, the rolling direction experiments serve as a fine example for the qualitative behavior of the transverse specimens, as well. There are however, more subtle quantitative differences in the strain fields of the two textures which will be explored in the next section.

SECTION 3.2: COMPARISON OF DEFORMATION IN TRANSVERSE AND ROLLING DIRECTIONS

Rolled nickel titanium sheet, the base material used for this dissertation, often develops a crystallographic texture, which can have a large impact on macroscopic superelastic response. As discussed in Chapter 1, the rolling direction tends to have a favorable texture resulting in larger recoverable strains and lower transformation stress, while the transverse orientation tends to have a larger transformation stress and lower recoverable strains. (Figure 3.2a) Previously it was assumed [43–48] that this discrepancy in transformation strains was due in large part to grain orientation, with the rolling direction having the higher concentration of grains oriented to maintain high transformation strains and more extensive martensite transformation. While the grain orientation argument holds for the average transformation strains of a rolling direction specimen, the extent of martensite transformation does not differ greatly between the favorable and unfavorable orientations.

The distribution of martensite transformation, insomuch as it can be inferred by local strain, is more similar in rolling and transverse direction samples than the accommodated axial strain might make it seem. A comparison of their local strain fields at the microscale (Figure 3.2bc)

36

shows how much more complete the transformation appears for the rolling direction sample. The transverse orientation looks sparse compared to the uniform high strain accommodation of the rolling direction image. However, analysis of the martensite fraction using methods discussed in Chapter 2 shows that both orientations have large amounts of martensite transformation throughout their microstructure. The rolling direction field of view maintains a 0.075 axial strain with 88.6% transformed martensite across the entire microstructure. The transverse field of view had only 0.05 axial strain with 85.95% of the microstructure transforming to martensite. The rolling direction also had a higher fraction of CV formation; 47.8% of the transformed martensite was in a CV configuration versus the transverse direction's 24.6%.

From the discrepancy in the CV volume fraction, we can see that much of the perceived difference in martensite transformation is attributable to the distribution of high-strain CVs distributed throughout the microstructure. The smattering of high strain CVs in the low strain HPV configurations present in the transverse microstructure mask the extent of martensite transformation, making it appear that it is suppressed compared to the higher strain HPVs in the rolling direction material. Both orientations displaying such extensive transformation on the microscale which is not directly associated with any easily identifiable microstructural features, indicates that statistical tools are needed to determine which features, if any, significantly influence martensite transformation.

SECTION 3.3: LOGISTIC FIT AND ANALYSIS OF TRANSFORMATION MODE

SEM-DIC and the full field methods paired with it produce large, detailed datasets with millions of points per analyzed image. Even considering a small portion of these sets is bound to include a large number of outliers and noise, making a deterministic feature-by-feature analysis problematic if not impossible. To circumvent this issue, simple statistical methods were used to

determine if any microstructural features were associated with more or less extensive martensite transformation, or if there were any detectable influences on the configuration of the transformed martensite.

Given the numerous available variables from the full field experimental techniques used for this dissertation work, a general and flexible statistical model was needed. In addition to accepting any number of input variables, the output of any regression function used to predict volume fractions of transformed martensite needs to be bound between 0 and 1 since volume fraction predictions outside this bound cannot exist. To this end a logistic regression [96] of the following form was used

$$p(x_1, x_2, \ldots x_n) = \frac{\exp(\beta_0 + \beta_1 x_1 + \beta_2 x_2 + \cdots \beta_n x_n)}{1 + \exp(\beta_0 + \beta_1 x_1 + \beta_2 x_2 + \cdots \beta_n x_n)} \tag{3.1}$$

Each input variable (x_i) is paired with a linear constant (β_i) which can be determined by doing a linear regression on

$$\ln \frac{p(x_1, x_2, \ldots x_n)}{1 + p(x_1, x_2, \ldots x_n)} = \beta_0 + \beta_1 x_1 + \beta_2 x_2 + \cdots \beta_n x_n \tag{3.2}$$

This is useful in terms of computational expediency, as the non-linear exponential function can be derived using linear methods.

Using the logistic fit in Equation 3.1 several combinations of local variables were applied to the local HPV fraction, CV fraction, and total martensite fraction maps. Point by point analysis using the most local variables—distance to grain boundary, kernel average misorientation, grain boundary axis-angle misorientation, m' misorientation of HPV habit planes—resulted in no significant trends or correlation with transforming volume fraction. This has two probable causes. First, the geometry used to calculate any geometry-dependent values was a 2-D section of the real 3-D structure. The grain sizes, grain boundary distances, and the true misorientation of grain boundaries are all dependent on the full 3-D geometry of each grain volume rather than the 2-D

slice provided by EBSD. Given a more columnar grain structure, this issue could be circumvented, but it is impossible to avoid with the nearly equiaxed microstructure examined here. Second, the multiplicity and low variance of fitting values could cause the lack of correlation. Within any grain, multiple points will have nearly identical input values, and due to the heterogeneity of subgrain martensite formation, can have completely different outputs. This leads to the fit becoming more of an average as there are not enough unique points to make a distinct trend along any one parameter.

There is little that can be done to address the geometry problems inherent to the available 2-D data set. However, by averaging each grain into a unique value before fitting, the issues of redundancy can be alleviated. This limits the fit in two major ways. First, the prediction is now more of a probability of transformation, rather than a fixed predictor of martensite transformation. Rather than the $p(x_1 \ldots x_n)$ output predicting the volume fraction of HPV or CV or martensite in a grain, it is instead set to represent the probability of any point in that grain transforming to one configuration or the other. For a large number of grains, this can be seen as equivalent to an expected value of martensite transformation. Second, it limits the predictors in this probability function to those that are not grain size or shape dependent. While multiple equivalent grain-averaged values are possible to use in this case, the analysis described here had the most success using the resolved shear stress on the habit and twinning planes of all the HPVs and their CV components, respectively. Despite this limited input set, there are still detectable trends in the propensity for CVs to form over the more compatible HPV structures.

When considering the grain-averaged values of resolved shear stress over the various CV and HPV configurations for all grain orientations a correlation can be made between increasing resolved shear on twinning planes and the propensity to transform into a CV configuration of

martensite. The fitted logistic functions for the Schmid-like factors for resolved shear on habit planes (HPV S.F.) and along twin planes (CV S.F.) are summarized in Figure 3.3 for data taken from all experiments used in this dissertation work. A strong positive trend can be seen between the expected fraction of CV transformation with respect to the resolved shear on twin planes. (Figure 3.3a) However, the propensity for HPVs to transform is much more weakly influenced by the resolved shear along habit planes. (Figure 3.3b) The negative trend in HPV fraction with increasing CV Schmid Factor is due to the exclusivity of HPV and CV fraction. Since the CV fraction has such a positive trend over the same range, it must come at the expense of HPV fraction. The overall probability of a grain to transform to martensite remains relatively flat across all Schmid Factor combinations (Figure 3.3c), which is unsurprising based on the previous observation of martensite fraction in both the rolling and transverse direction samples.

The relative strength of the CV over the HPV dependence on resolved shear is indicative of the complexity of a nickel titanium habit plane over the twin planes. The internal twin planes of an HPV are crystallographically sharp and determined by the superposition of two rotationally related crystal lattices. In the case of Type I twins the planes are rational by definition, while the irrational planes in Type II twins have been shown to be composed of individual rational plane steps. [97–99] In both cases, any small perturbation from the sharp interface between the martensite variants will have a clean path to propagate across, making for reorientation of variants within the twin relatively easy. By comparison, the habit plane between the martensite and austenite twin is ultimately an elastic zone masking the only-on-average compatibility between austenite and the correspondence variant pair which forms the HPV structure. A small outgrowth of martensite into the austenite has a much more difficult time propagating as the elastic zone can effectively buffer any new mismatch it generates. Ultimately this means that twin planes are much

more sensitive and responsive to applied shear than the habit planes which makes sense from a very local crystallographic perspective.

Although it was not possible to determine all of the local determining factors of martensite transformation, how shear stress resolved on particular crystallographic planes was shown to probabilistically govern the selection of martensite configuration. Despite not being able to fit a deterministic function to predict local transformation based on all of the available microstructural features, the question of whether it is possible to find such a function is still somewhat open. A common assumption in the modeling of the transformation behavior of nickel titanium is that similarly oriented grains transform similarly. Since the full 3-dimmensional grain orientation is difficult to parameterize into a single scalar value, and was therefore not explicitly included in either the local or grain average fits, its influence over variant selection in martensite transformation is not addressed with the statistical fits performed here. The assumption that grain orientation is sufficient to determine transformation behavior will therefore be examined in the next section.

SECTION 3.4 COMPARING TRANSFORMATION CHARACTERISTICS OF SIMILARLY ORIENTED GRAINS

In this section grain similarity is first defined. Following this, the relationship between the martensitic transformation of a grain and its crystallographic orientation is presented from analyses of the strain maps derived in the SEM-DIC studies. Specific attention is paid to transformation extent and heterogeneity as they relate to grain orientation.

Grains were categorized by the orientation of each austenite crystal along the loading axis of the sample. Two grains, G1 and G2, were designated as having the same crystallographic loading axis if a rigid body rotation of G1 about the sample loading axis matched the orientation of G2 after taking into account all symmetry operators (Figure 3.4). A small range of deviation (θ

≤ 5° or 2.5° depending on orientation population) of loading orientations from a low index direction was used to bin grains into similarly oriented groups in the analysis, as perfect alignment was improbable in a real material. One benefit of this rotation-based definition for grain orientation similarity is the lack of any change to strain measurements along the rotation axis, which in this case was the loading axis. Preserving strain values along the loading axis by implementing this definition of grain similarity was necessary to directly compare experimental measurements of transformation strain with phenomenological predictions of martensitic transformation. Maps of the maximum strain predicted in single crystals with different loading axes can readily be found in the literature [33,43,100] (Figure 3.5a). Direct comparison can be made between polycrystals, which are essentially comprised of constrained single crystals, and unconstrained single crystals. Note that comparing strains along axes other than the loading axis is not straightforward in these experiments. Rotations about the loading axis can align off-axis orientations, but DIC-obtained strain measurements cannot be similarly reoriented. Two-dimensional SEM-DIC cannot measure out of plane strain; thus arbitrarily rotating the strain field to match the rotations required to align crystal orientation is generally not possible.

When determining whether two grains have undergone equivalent martensitic transformation it is not sufficient to compare a single value, such as the mean strain ($\bar{\varepsilon}$). Averaging transformation strain over the grain surface area obscures fundamental differences in the spatially resolved martensitic transformation behavior. To illustrate this point, Figure 3.6 shows three grains with similar crystal orientations that have undergone martensitic transformation. Grains B and C have similar mean values of strain, but different strain heterogeneity and thus arguably different martensite morphology. Grain B has a uniform distribution of strain, and by inference martensite distribution, while Grain C has two high strain martensite laths in a low strain austenite matrix.

Grains A and B have similar strain ranges (indicative of similar levels of heterogeneity across the grain), but different mean values and overall strain accommodation. In this work, the strain in each grain is characterized by hundreds to thousands of measurement points for a statistically relevant distribution of grain behavior (strain magnitude and heterogeneity).

Grains can contain austenite and martensite delineated by a sharp boundary, as shown in Figure 3.2. Grains with sharply delineated martensite lathes tended to show larger ranges of minimum and maximum strain, while grains with higher transformation homogeneity showed narrower ranges. This makes sense if one considers each phase and/or variant to produce a narrow range of stains. Under that assumption, when one grain is comprised of one variant, or a homogenous mix of multiple variants with a feature length below the detection limits of SEM-DIC, then a single, tight strain distribution is expected. However, if several regions of a grain each transform to a different variant (or variant mix), these several distributions will sum to a much wider spread across the entire grain.

To remove the effects of data outliers or erroneous points, the limits of the upper and lower quartiles (the middle 50%) of strain data for each grain were used to define its transformation strain range. While not a direct measure, this strain range is a reasonable way to evaluate transformation homogeneity across a large number of grains. Mean strain values of each grain are not sensitive to these heterogeneities and can thus provide data on the overall degree of transformation in each grain, with higher strains indicating a higher volume fraction of martensite.

Using two metrics — mean strain and strain spread — measured in each grain, it is determined that grains of similar orientation do not transform similarly. The chosen metrics were confirmed to correspond with mean transformation volume fraction and transformation heterogeneity for maps of local transformation strain of a small test group of similarly oriented

grains. The sampled population was then expanded to include all those grains with small deviations from low-index orientations. In both populations, no causal link between orientation and extent of martensitic transformation was detected.

Models based on the phenomenological theory of martensite formation [30,37,51,52,100–105] base their macroscopic stress-strain predictions on the assumption that grains with the same orientation, including those related by crystallographic symmetry, produce the same transformation strain in a polycrystalline material. However, in this work it was found that neither grain orientation nor grain size significantly affected either the mean strain or the strain range of individual grains. While averaging single crystal properties across a field of view containing approximately 5000 grains produced roughly correct trends in the macroscopic strain (Figure 3.5b), predicting transformation from single crystal properties did not produce the correct mean strains inside of each grain and did not capture the wide range of strain they can encompass. Grains can have a large degree of heterogeneity, as seen in Figure 3.6a, which is not addressed by taking single crystal properties. In addition, predictions using the single variant assumption can deviate significantly from experimental results in both the averaged response of individual grains and the average transformation strain measured across all grains in the sampled microstructure. The experimentally observed mean strains of grains deviated by up to 0.097 from those predicted by assuming transformation of the most favorable variant throughout the grain (see the marked grains in Figure 3.7). In the field of view shown in Figure 3.7, the difference between the mean axial strains ($\overline{\varepsilon_{xx}}$) of the predicted and experimental fields was 0.031. This difference was also observed for other specimens tested, both for specimens machined in the rolling direction and transverse to the rolling direction.

Mean strain and strain range were used to compare the transformation behavior of individual grains. Let us first consider the mean strain. Averaging axial strain over each grain instead of measuring the spatial distribution of transformation — such as the number or spacing of martensite laths— produces a single value for comparison to theoretical predictions. Although it is clear that grains do not transform uniformly, but rather can contain a large degree of heterogeneity, this averaging is performed in order to compare experimental results to theoretical predictions that do not account for heterogeneous transformation. The observed transformation heterogeneity in grains, the discrepancy between experimentally measured and theoretically predicted mean strains, and the discrepancy in mean strains between grains of similar orientation are all strong arguments against the validity of assuming transformation similarity based on similar grain orientation. Grains with different mean strain values must have different martensite transformation paths — constituting both the variants and final volume fraction of martensite transformation. In the microstructures examined here, mean grain strain and transformation area fraction exhibited a fairly linear trend (Figure 3.8), indicating that two grains with similar mean strain values often have similar volume fractions of martensite variants and retained austenite. Points were determined to have transformed to martensite if they achieved >50% of the predicted twinned transformation strain—which was taken as an indication they were at least half martensite by a rule of mixtures approach. Volume fractions for each grain were determined by averaging the binary values for each point in the grain. Using this definition, all of the 26 grains with a 49-51% martensite volume fraction showed a narrow range of grain averaged strain ($\overline{\varepsilon_{xx}}$ = 0.028-0.038). The converse does not hold, however, as the same strain range ($\overline{\varepsilon_{xx}}$ = 0.028-0.038) contained 258 grains with a mean martensite volume fraction lying at 60%. Simply considering the mean behaviors of grains is not sufficient to show a general trend in similarity.

We observed that similarly oriented grains can exhibit large variations in mean strain. An example is shown by the two grains marked A and B in Fig. 4a. The bar graphs on top of each grain represent the experimentally measured strain values over that grain surface. As approximately 5.5 million measurements were made over 5300 grains, each grain had nominally 1000 measurements. The middle 50% of the strain data is denoted as the thick bar. The 95th percentile bounds are denoted by thin bars. Open circles in the middle of the distribution mark the mean strain of the grain and the median is marked with a crossbar. These grains, despite similar orientations, accommodated significantly different overall strains, with grain A accommodating a much higher mean strain than grain B.

Strain range is indicative of transformation heterogeneity, where a small strain range indicates relatively homogeneous transformation in that area. Grains that fully and uniformly transformed had a narrow strain range, while grains with clearly defined martensite plates and/or untransformed austenite had a larger strain range. The experimentally measured strain ranges of individual grains showed significant variation. Some grains exhibited strain ranges of +/- 0.1%, indicating relatively homogeneous transformation, while in other grains the strain values spanned a range nearly two orders of magnitude larger. These large strain ranges within a single grain are contrary to the phenomenological assumption of complete and homogenous transformation that would result in uniform strain.

The strain range (transformation heterogeneity) of individual grains did not depend on grain orientation or on their mean strain. Similarly oriented grains could exhibit large variations in strain range, as shown by the two grains marked B and C in Figure 3.6a. These grains had strain ranges of 0.043-0.055 and 0.033-0.060 respectively, despite sharing a loading axis of [0.8179 0.5579 0.1404] to the fourth significant digit. Grains with similar mean or median strains also did

not necessarily have similar strain ranges. For example, again consider Grains B and C in Figure 3.6. These two grains had nearly identical median strains, but very different ranges of strain values contained within their surface boundaries. A pair of martensite laths cutting through Grain C as well as an area of untransformed material along the side of this grain account for the wider strain range. When averaged, the heterogeneities in Grain C match the more uniform deformation in Grain B. Considering the width of the strain distribution of each grain reveals differences transformation heterogeneity in the two grains.

To examine transformation strain and heterogeneity with respect to crystallographic orientation, the full-field strain data at the microstructural length scale was segmented into grain-by-grain strain distributions. Each bar in Figures 3.7-3.10 represents the experimentally-measured surface strain values over grain from the field of view shown in Figure 3.1d. Similar to Figure 3.4, the middle 50% of the strain data is denoted as the thick bar, the 95th percentile bounds are denoted by thin bars, the median of each distribution is marked by a crossbar, and open circles mark the mean strain of the grain. The grains were sorted along the x-axis by the misorientation between the [hkl] crystal axis and the sample loading axis. Each grain was color coded by grain size, given as total number of data points contained inside the surface of the grain, showing that there is no apparent effect of size on strain distribution.

Favorable orientations for transformation were examined, including the {111} (Figure 3.9), {355} (Figure 3.10), and to a lesser extent the {110} (Figure 3.11) families of the parent austenite phase. Comparison within and between each of these families shows that the phenomenological assumption that each family of grains has a constant transformation strain does not hold for polycrystals. To determine this, the mean strain and strain range of each grain was normalized by the predicted strain of the austenite-to-twinned-martensite transformation for that grain orientation

[100,106], allowing comparison between different orientations. With each of these orientations, there was a wide variation in the mean strain of individual grains in the polycrystal. Although a large portion of the mean strain values fell within 20% of the predicted orientation-dependent axial strains for twinned martensite [100,106], outliers did occur. It is important to note that even if these outliers are eliminated, a wide range of transformation strains persists, indicating that final martensite configurations do not solely depend on grain orientation. Even for grains with distributions within 20% of the predicted transformation strain, it was possible to find two distributions that shared no overlap between their 95th percentile bounds. Two grains without overlap have distinctly different configurations of martensite in their fully transformed state that lead to completely different strain distributions. Moreover, neither grain size nor misorientation from the preferred crystal axes significantly impacted these values. Finally, these findings were not isolated to orientations favorable for transformation; for example, grains with a {100} (Figure 3.12) orientation along the loading axis also showed significant variation in their mean strains with little dependence on grain size or misorientation.

Nor is it the case that favorably oriented grains exhibited a higher degree of homogeneity. The {100}, {110}, {111}, and {355} grain families all showed a similar spread in strain distribution, but exhibited different mean strain values. From the experimentally measured, orientation averaged IPF map in Figure 3b, it is determined that the {100} grains had a much lower transformation strain when averaged together as compared to the {110} and {111} grains. However, considering each grain in this family individually in Figures 3.9 and 3.11, one can see grains exhibiting transformation strains well above the low collective average. Moreover, the same range of strain spread can be seen in each family of grain orientations. Tracking the strain spread across all orientations (Figure 3.13a) and grain sizes (Figure 3.13b), indicates that the

48

heterogeneity does not strongly depend on either orientation or grain size. Despite some trends in mean strain existing across an inverse pole figure (see Figure 3.5b), plotting the mean strain spread for the same orientations yields the uniform distribution as seen in Figure 3.13a. Thus, unlike mean strain, the strain range (degree of transformation heterogeneity) did not have a significant dependence on grain orientation. The strain range (degree of transformation heterogeneity) of individual grains also did not depend on the grain size. Wide and narrow spreads of strain values were seen in both large and small grains, as shown in Figure 3.13b and also evident in in Figures 3.9-3.12.

SECTION 3.5: SUMMARY

Martensite transformation in a polycrystal is a complex phenomenon not solely dependent on the orientation or size of independent grains. From this analysis it is clear that grain orientation alone is not sufficient to fully predict the path of transformation during superelastic deformation. Grains of similar orientation show massively different strain accommodation and attempts to fit regressions to the spread in their behavior were not successful. It is evident that a more complete picture of the surrounding microstructure and the specific interactions of grain neighborhoods are required to accurately predict the specifics of transformation in polycrystalline SMAs.

However, despite the difficulty of accurately predicting the complete path of martensite transformation, the experimental data gathered here has revealed a simple trend in the propensity of martensite to transform to a correspondence variant configuration. Increasing resolved shear on the twin plane of a habit plane variant will promote the reorientation of its component correspondence variants to a volume fraction which is incompatible with the parent austenite. To the best of the author's knowledge, this dissertation work is the first time such an incompatible configuration of martensite has been directly observed in a recoverable martensite structure. What

49

remains to be examined, however, is the impact of this incompatibility on subsequent transformation and recovery in the polycrystal. Tracking the accumulation of residual strain and relating it back to the configuration of martensite in the initial transformation will be covered in the next chapter, where it will be shown that the correspondence variants measured here play a key role in the cyclic damage accumulation in these polycrystalline structures.
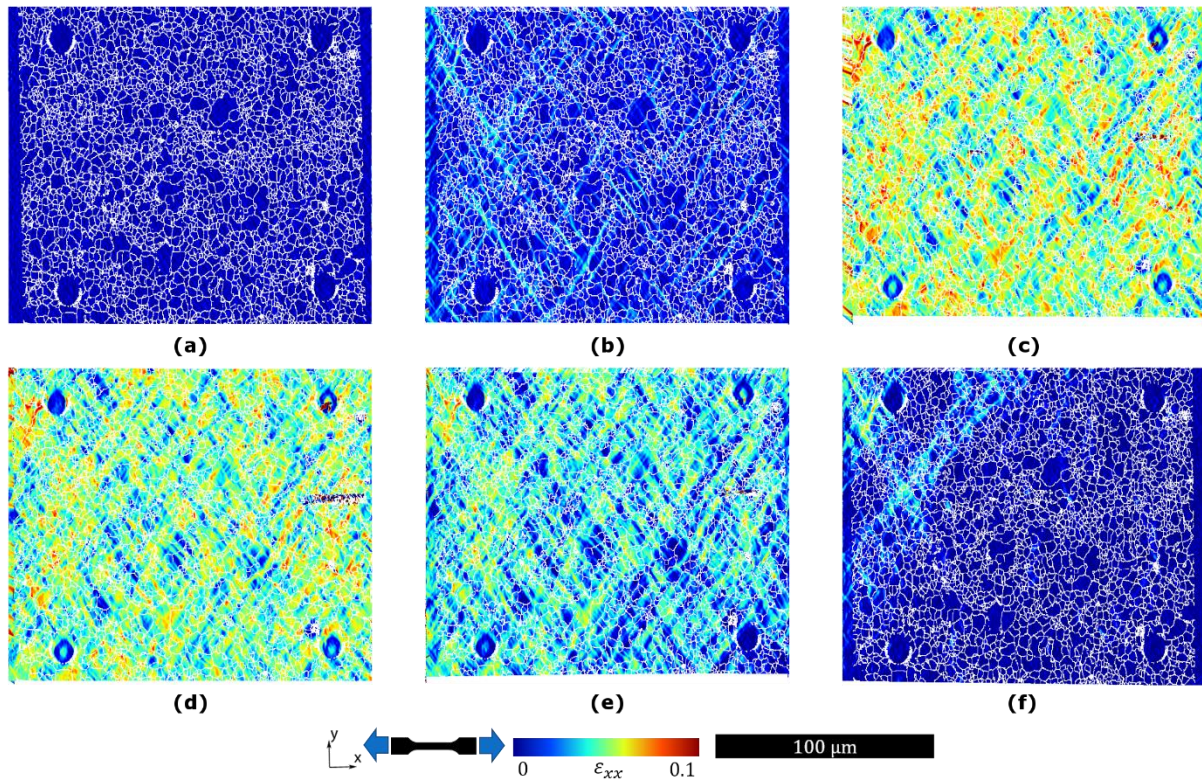
Figure 3.1: Local axial strain maps showing the progression of martensite transformation through a super elastic cycle. The images are in time sequence from elastic strain (a), through initial transformation (b), fully saturated martensite (c), elastically unloaded martensite (d), initial recovery (e), to final remnants of martensite band (f). The white lines are grain boundaries measured from EBSD.
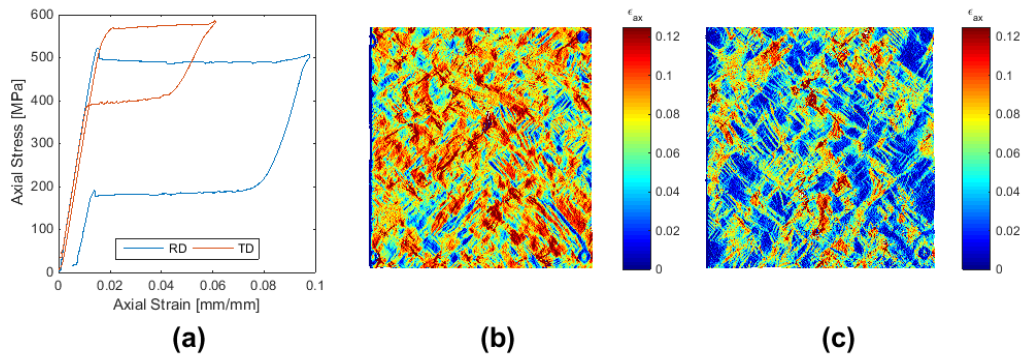
Figure 3.2: (a) Macroscopic stress-strain curves for rolling (RD) and transverse direction (TD). The local axial strain maps of the rolling direction (b) and transverse direction (c) specimens that generated the stress-strain curves are also show.
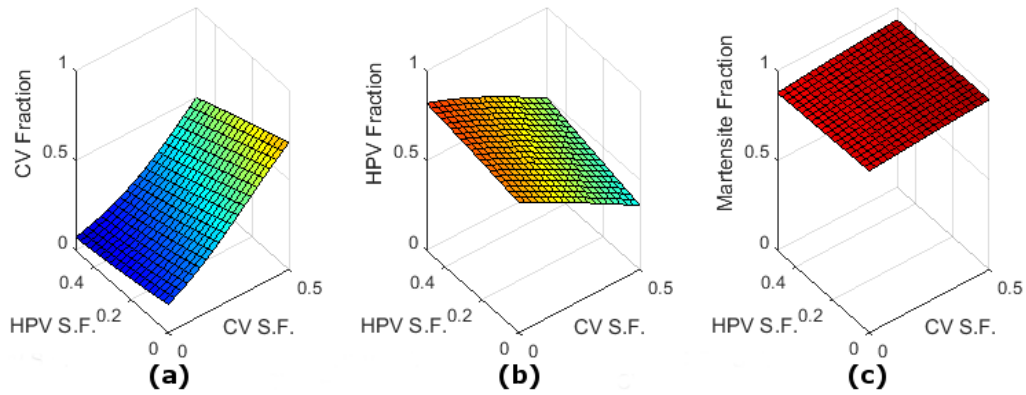
Figure 3.3: Logistic fits of expected martensite fraction in the CV (a), HPV (b), and general martensite configurations (c) based on the resolved shear stress on the habit plane (HPV S.F.) and twin planes (CV S.F.).
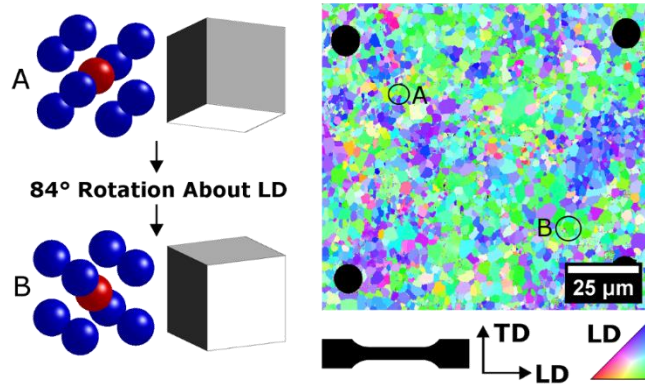
Figure 3.4: Schematic showing the isomorphism of two grains with similar loading direction orientations. Any two grains with similar loading axes can have their orientation mapped to one another by a rigid rotation about the loading axis, which has no effect on the measured loading axis strain.
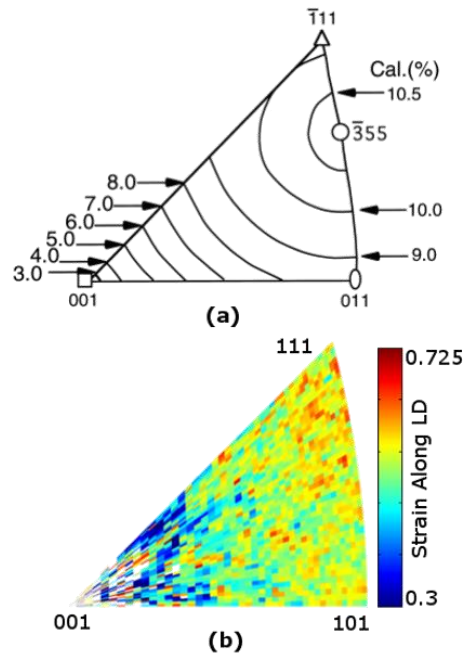
Figure 3.5: (a) Inverse pole figure (IPF) map of accommodated strain from martensite transformation based on loading direction of single crystals from [10]; and (b) polycrystalline SEM-DIC data from these experiments. The overall trends of low strains along {100} directions and highest strains along {111} directions remain intact. However, the measured polycrystalline strain shows ~3% less strain over much of the IPF space.
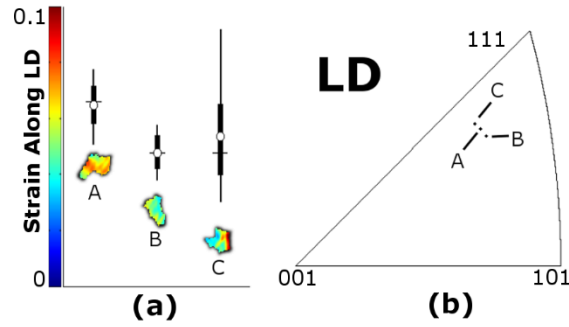
Figure 3.6: (a) Selection of strain distributions from three grains with similar orientations as shown in (b). The thick line represents the middle 50% of data and the thin line constitutes 95th percentile bounds for each grain. The median of each grain's strain distribution is marked with a crossbar while the mean is shown as an open circle. A and B show the same level of homogeneity (strain spread) despite different mean/median strain levels, while B and C show the same median strain with C showing much larger heterogeneity of transformation.
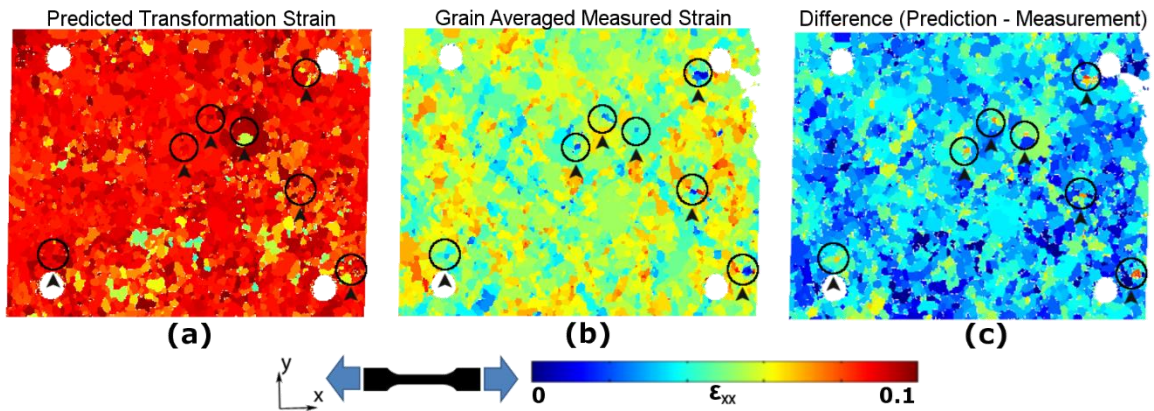
Figure 3.7: (a) Predicted transformation strain from phenomenological theory; (b) experimentally-measured strains; and (c) the difference between (a) and (b). Grains with the highest deviation between predicted and measured transformation strain are circled in each field. Summaries of the strain fields are given in Table 3.1.

	Predicted Transformation Strain (Single Variant)	Measured Transformation Strain (Grain Averaged)	Difference
Mean	0.085	0.054	0.031
Max	0.105	0.104	0.097
Min	0.033	0.003	-0.037

Table 3.1: Summary of full field strain maps from Figure 5.
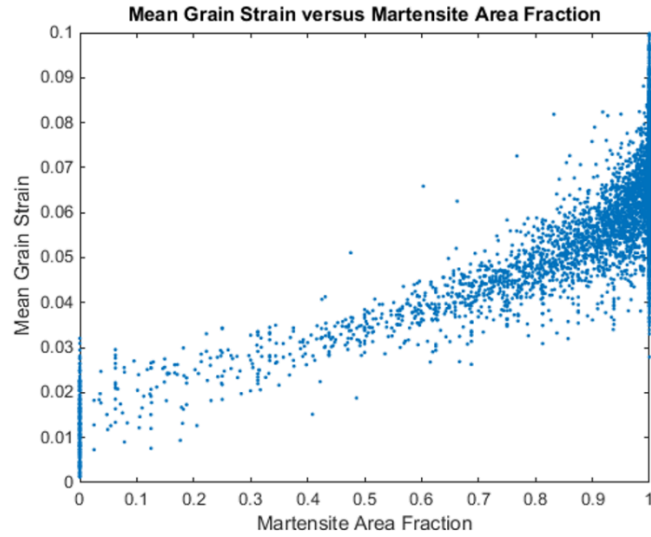
Figure 3.8: Mean axial strain in the grain as a function of martensite area fraction. Points were partitioned into austenite or martensite using a rule of mixtures approach. Twinned martensite strain in each grain was calculated; if the measured axial strain at a point was closer to the twinned strain than the nominal elastic strain ($\varepsilon_{xx} = 0.01$), the point was considered to be fully martensite. Binary states were then averaged to determine the martensite area fraction of each grain.
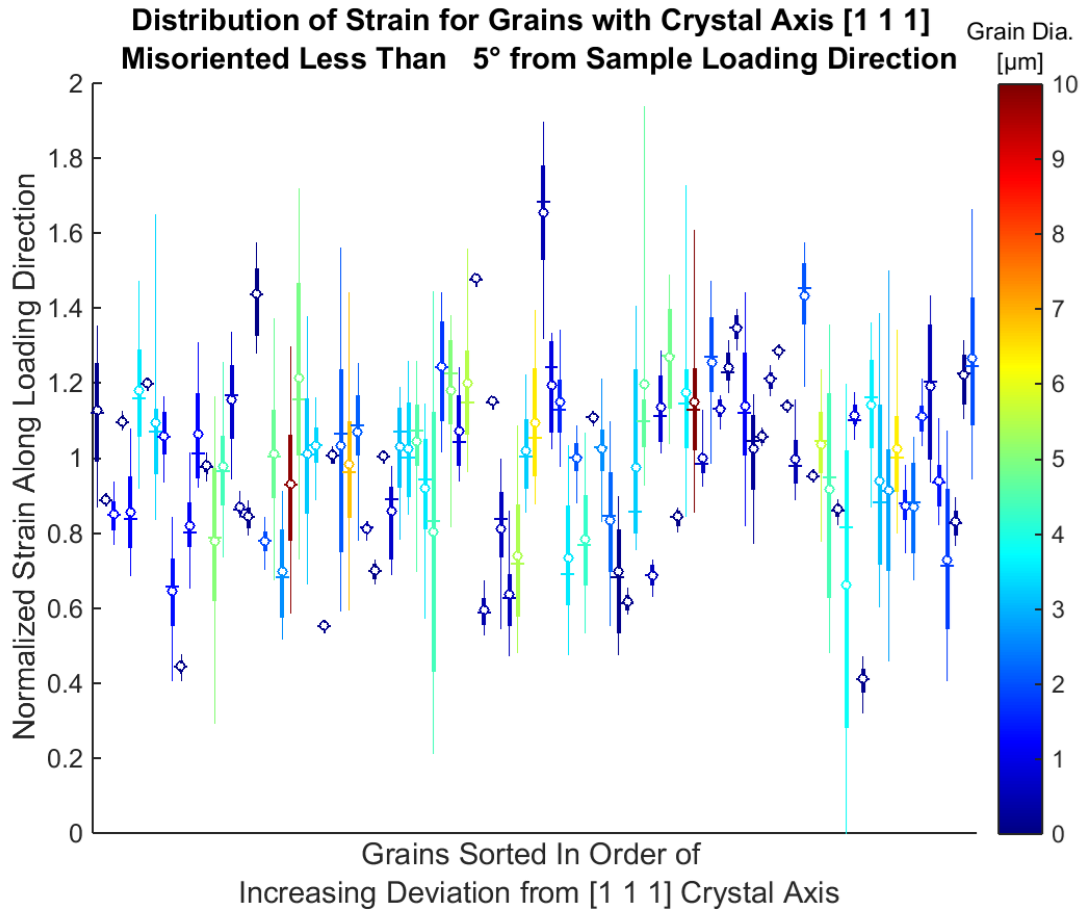
Figure 3.9: Individual grain strain distributions for grains with loading axes oriented along [111]. To facilitate comparison between the different orientations, all strain values were normalized to the predicted transformation strain of twinned martensite, which is dependent on the crystal orientation. To limit clutter in this image, grains with a diameter of less than 0.5 µm were omitted.
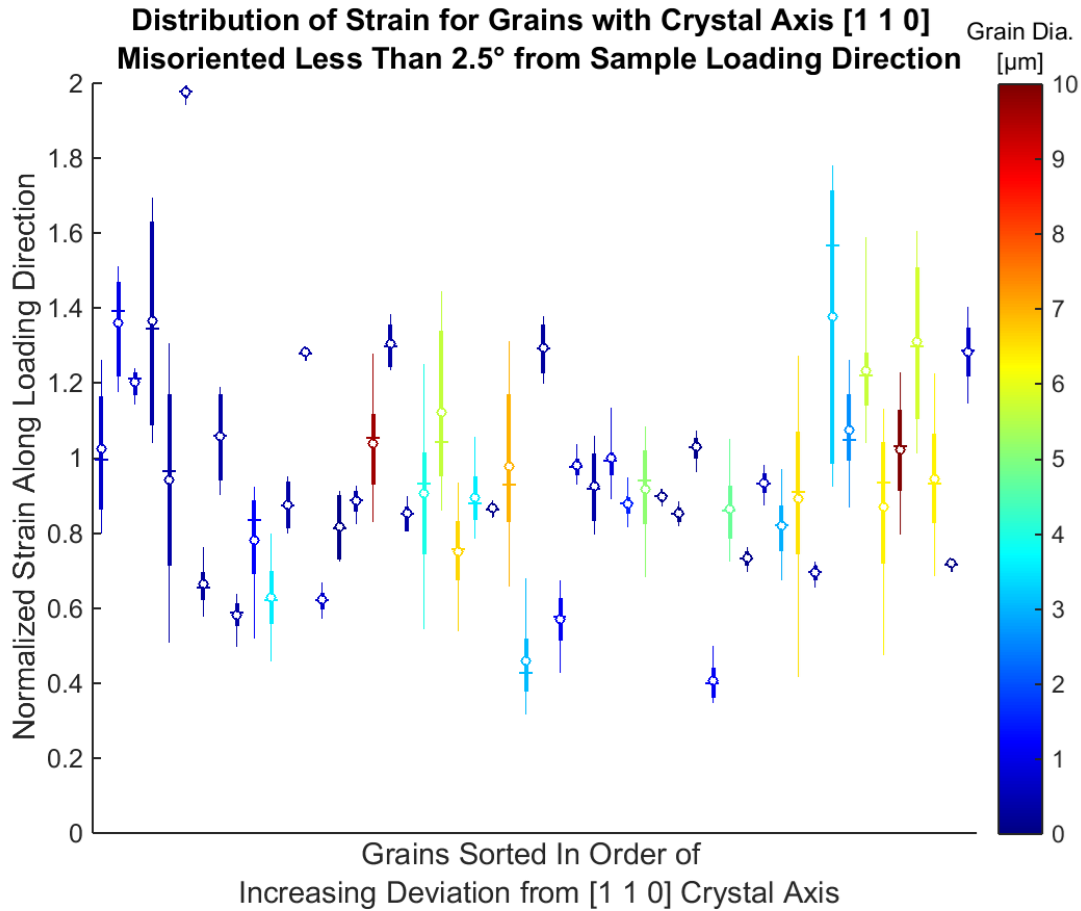
Figure 3.10: Individual grain strain distributions for grains with loading axes oriented along [110]. To facilitate comparison between the different orientations, all strain values were normalized to the predicted transformation strain of twinned martensite, which is dependent on the crystal orientation. To limit clutter in this image, grains with a diameter of less than 0.5 μm were omitted.
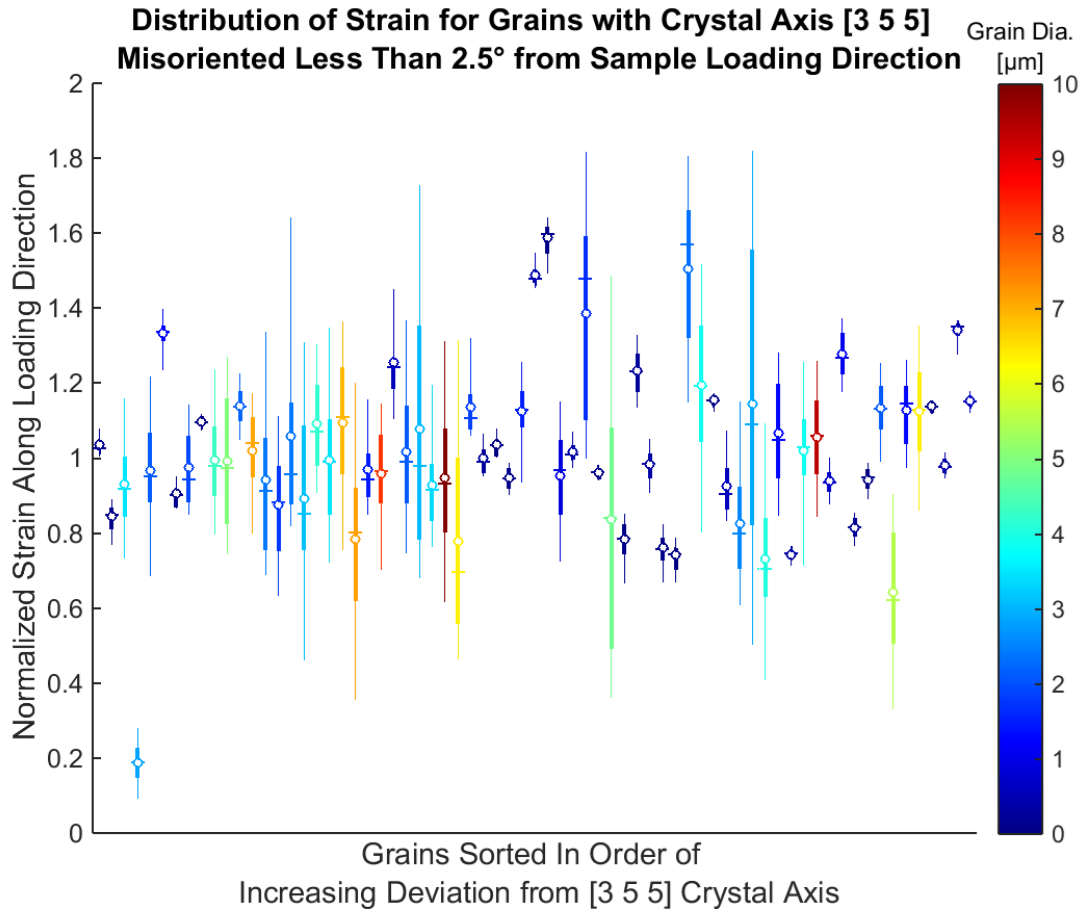
Figure 3.11: Individual grain strain distributions for grains with loading axes oriented along [355]. To facilitate comparison between the different orientations, all strain values were normalized to the predicted transformation strain of twinned martensite, which is dependent on the crystal orientation. To limit clutter in this image, grains with a diameter of less than 0.5 µm were omitted.
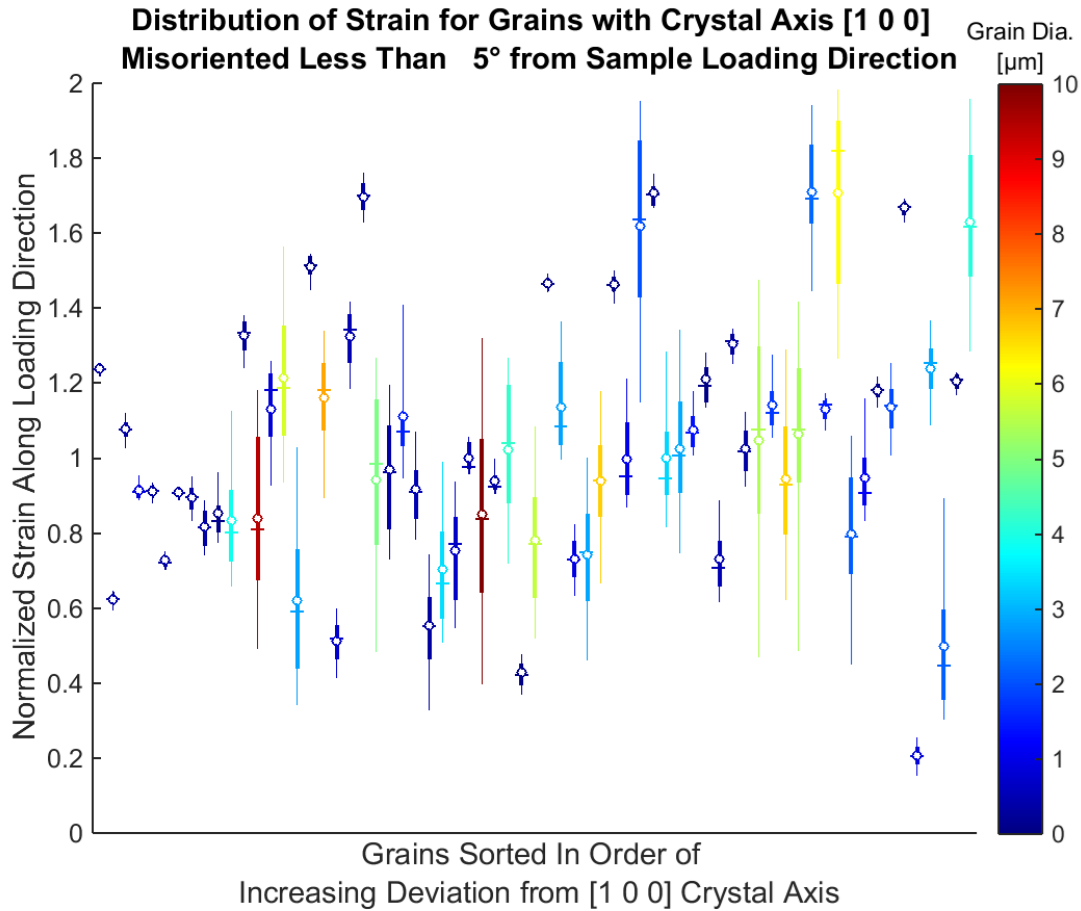
Figure 3.12: Individual grain strain distributions for grains with loading axes oriented along [100]. To facilitate comparison between the different orientations, all strain values were normalized to the predicted transformation strain of twinned martensite, which is dependent on the crystal orientation. To limit clutter in this image, grains with a diameter of less than 0.5 µm were omitted.
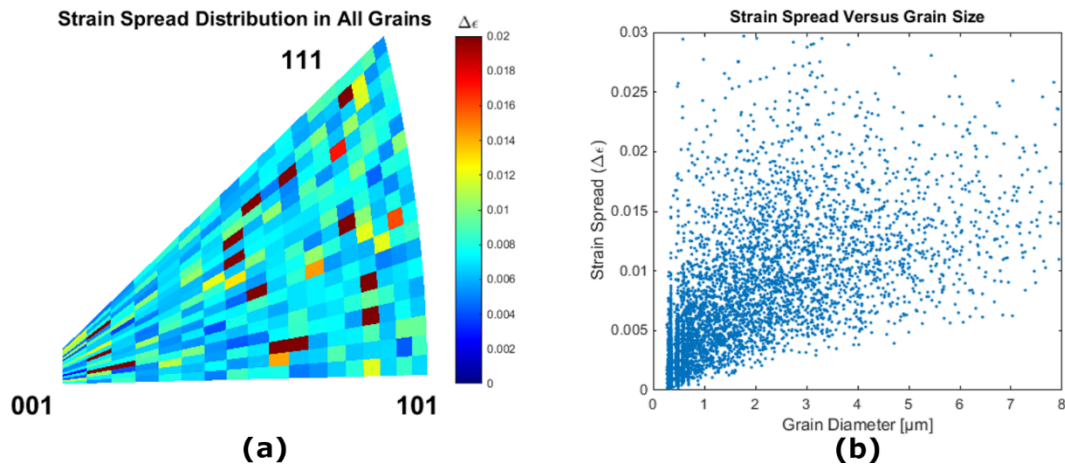
Figure 3.13: Strain spread of grains is not controlled by (a) loading axis orientation or (b) grain size. The same mean strain spread can be seen for most orientations in (a) with no trends across the orientation space. Similarly, comparing the grain size and strain spread of each gran in (b) yields no trend beyond an increasing lower bound in strain spread for larger grains. However, the same strain spreads observed in the largest grains can be found in a large number of smaller grains as well. Additionally, it is unclear if the lower bound is a true trend or a consequence of the larger number of sample points in the larger grains.

CHAPTER 4: ACCUMULATION OF RESIDUAL STRAIN IN INCOMPATIBLE MARTENSITE

In Chapter 3, a propensity for martensite to take on a correspondence variant (CV) configuration in single cycle experiments was identified. Transformation to this configuration of martensite, which has not been previously documented in the literature, raises significant questions about how phase compatibility plays a role in the observed accumulation of residual strain in superelastic nickel titanium. In this chapter, the necessity of including CV configurations in order to explain the large recoverable strains experimentally measured in the microstructure with SEM-DIC is shown. By tracking transformation across multiple superelastic cycles it is also determined that residual strain accumulates more quickly in CV regions. Additionally, a positive linear correlation between residual strain accumulation in the microstructure and the loss of actively transforming martensite in later cycles was determined. In total, the accumulation of residual strain and the loss of transforming volume fraction leads to a remnant network of locked-in martensite and plastic deformation that helps to determine the stable configuration of later cycle superelastic transformation.

SECTION 4.1: INCOMPATIBLE PHASE MIXTURE IN INITIAL TRANSFORMATION

Processing the SEM-DIC strain fields of several superelastic specimens using the martensite matching algorithm presented in Chapter 2 indicates that regions of CVs coexisted with regions of untransformed austenite and HPVs in individual grains throughout the microstructure. Additionally, these CV regions formed in the microstructure early in the superelastic cycle, well before the end of the macroscopic stress plateau. Prior experimental work [107] suggests that

61

significant reorientation of martensite variants does not occur until later in the superelastic deformation process, when the stress begins to rise above the transformation plateau. Interestingly, it has generally been assumed that CVs do not form before this reorientation process, as they are incompatible with the parent austenite. However, by looking at the possible permutations of which martensite configurations are included in the martensite fitting algorithm, it is possible to show that the existence of CVs in the initially transformed microstructure is necessary. An example grain is shown in Figure 4.1 to compare the actual strain measurements with fits that omit or include the presence of CVs in the fitting algorithm. If the analytical fit is limited to single and multiple HPV solutions (Figure 4.1b), significant differences with the experimental data arise. Specifically, HPV solutions can be found for data points with ≤ 0.06 axial strain, but the algorithm fails to account for regions that reached upwards of 0.1 axial strain. Including the possibility of CVs in addition to the HPV solutions (Figure 4.1c) results in a strong match to the measured strain fields. The necessity of including CV transformation modes to describe the experimental behavior is a strong indication that they form in the early stages of superelastic transformation. HPVs alone are not able to account for the large recoverable strains in the first superelastic cycle.

Analysis of the local strain fields in the first cycle indicates that large amounts of material transformed to CVs and recovered to austenite, as shown in the first bar of the plot in Figure 4.2 which tracks the phase mixture across a ten cycle experiment. The first superelastic cycle showed the greatest recoverable strain, both in the macroscopic stress-strain response and in the grain-level SEM-DIC strain fields. As cycling continued, the volume fraction of recoverable CV decreased in most areas – rapidly in the early deformation cycles, and later more slowly as the microstructure stabilized – giving way to an increase in HPV volume fraction. The nominally five or six cycles needed to stabilize the CV fraction, as shown in Figure 4.2, corresponded to the time taken to

stabilize both the global and local responses, including the rate of shakedown in the macroscopic stress-strain response which can be seen in the rapid change and later in the stability of the stress-strain curves in Figure 4.3a.

The correlation between the macroscopic strain response and evolution of transforming martensite configuration makes sense if one considers that the former is ultimately the sum of the latter. As the high transformation strain CV configurations are lost or locked into the microstructure, the total amount of available recoverable strain is reduced to the remaining HPV configurations. While they produce less recoverable strain, these HPV configurations appear to be more stable from both the macroscopic strain response and the phase fraction tracking. The variability of stability in different martensite configurations points to a potential optimization path for maximizing either transformation strain or the stability of the superelastic stress-strain response in shape memory alloys. Alloy composition and orientation which promotes CV formation will maximize the total transformation strain during the first cycles, but will quickly lose these properties as the martensite gets locked into place. Alternatively choosing a microstructure that heavily preferences HPVs can lead to greater stability in the stress-strain response. In fact, the latter possibility has recently been explored in ternary nickel titanium copper alloy films. [108] The large volume fraction of compatible precipitates heavily favors and accommodates HPV transformation and the shakedown is minimized. However the large volume fraction of non-transforming precipitate structure prevents large recoverable strains from being realized in the alloy. Whether similar techniques can be applied to bulk alloys while maintaining some level of reasonable transformation strain remains to be seen but the thin film work does corroborate observations in this dissertation work.

When a strict history assumption (for a description of the strict history and history free assumptions referenced here, see Chapter 2) was used to match martensite transformation in later cycles, 81% of the retained strain was attributed to the loss in transforming CV fraction. The remaining locked-in strain was likely due to plastic deformation, as the recoverable strain from HPVs increased during the same period. In contrast, if a history-free assumption was used, the residual strain had no apparent dependence on the loss of martensite in the CV-attributed points; across all strains attributed to a CV configuration, the residual strain remained a constant 0.03 axial strain. In this case, most of the loss in CV volume fraction was attributable to reorientation of the CVs into HPV configurations. The reasons for the difference between the strict history and history-free analyses are addressed in Section 4.3.

SECTION 4.2: ACCUMULATION OF RESIDUAL STRAIN IN CORRESPONDENCE VARIANTS

Areas that initially transformed with a higher CV fraction tended to accumulate greater amounts of strain in subsequent cycles. The accumulation of residual strain can be parsed onto a ternary diagram of Austenite-HPV-CV space for each cycle to demonstrate the phase dependent strain accumulation. This 2-D representation is shown in Figure 4.3d. However, even for a 1-D representation, as seen in the plot of residual strain against CV volume fraction from the initial transformation cycle in Figure 4.4, there was a positive relationship between the volume fraction of CVs and the accumulated residual strain in each cycle. Regardless of how it is represented, the trend between accumulated strain and CV transformation fraction was approximately linear, and the total residual strain tended to saturate in later cycles. A possible explanation is that CV formation and recovery is not as favorable a mechanism as HPV formation and recovery.

The accumulation of residual strain in the regions with higher CV fraction can be explained in context of the lack of compatibility between austenite and single CVs. While HPVs can maintain

an interface between austenite and transformed martensite, no such interface can be maintained between a pure CV and austenite. As there is no solution to the compatibility equation (Equation 1.3) between austenite and any orientation of CV, there must be some additional strain required to maintain compatibility between the two phases. Large zones of elastic accommodation (such as those bridging austenite and martensite in the HPV structure) or plasticity are likely candidates for maintaining the finite strain required for compatibility across the Austenite-CV interfaces. Given that initial transformation is largely recoverable, with significant residual strain only appearing in later cycles, there is likely an evolving combination of mechanisms at play in maintaining compatibility of the CV configurations with the parent austenite. From previous TEM work [36,57,69] examining the multiplication of dislocation structures in superelastic SMAs, it is likely that whatever small amount of plasticity is required to maintain the initial compatibility of transformation eventually multiplies and eclipses any other mechanisms that were initially active. The TEM micrographs produced from micropillars with varying numbers of applied compression cycles [36] showed a clear multiplication of residual dislocation loops left in the wake of martensite transformation. Although the martensite in those cases was attributed to a pure HPV configuration, the experiment demonstrated the tendency for dislocations to be dragged along by the austenite-martensite interface. If another dislocation structure was at play in maintaining the Austenite-CV interface, one would expect an equally strong tendency for dislocation-interface interactions.   The fact that at maximum only 80% of local residual strains can be accounted for with loss of transforming martensite volume fraction also supports the idea that additional plastic strain is established with cycling. The permanent plastic deformation produced by compounding dislocation networks seems the most plausible candidate to account for the missing 20% of the measured residual strain as well as the mechanism for stabilizing the retained martensite against

65

reverse transformation. However confirmation of this fact will require additional experiments involving high resolution TEM, as addressed in Section 5.2

The linear relationship between CV fraction and residual strain accumulation indicates a continuous breakdown of the habit plane compatibility between the austenite and martensite phases. As a HPV moves away from the prescribed ratio of component CVs toward a pure CV configuration, there is a continuous increase in the additional plastic deformation required to maintain compatibility with the austenite phase. This is due to the finite strain incompatibility between austenite and CVs and the compatibility between austenite and HPVs. An increasing fraction of CV that moves away from the HPV combination incurs a linearly increasing incompatibility strain (according to Equations 1.5 and 1.6) until the sample is 100% CV. Another way to consider this is that every unit of CV can be matched to the parent austenite by plastically deforming the austenite by a fixed amount. For every unit of transforming CV, a corresponding unit of plasticity must be developed in the austenite. A linear trend would develop from this type of accommodation since there would be a fixed ratio between the CV transformation volume units and the finite plastic deformation accommodation units. The experimental observation of a linear relationship between residual strain and initial fraction of CV in the recoverable transformation supports the rule of mixtures approach and finite accommodation approaches taken here.

Compositions which include additional CV fractions are likely to segment and deviate from the smooth habit plane of HPVs. This leads to a question of whether the accumulation of residual strain is solely caused by maintaining compatibility between austenite and the present martensite configurations, or has something to do the interface geometry. The presence of multi-HPV configurations of martensite provides a way to test the effects of interface geometry on residual strain accumulation. Any composition that can be created from the two compatible HPVs can

maintain a compatible interface with the parent austenite, though it may be serrated depending on the HPV geometry. The recovery of configurations which include CVs is impeded with increased cycling, but martensite configurations that include only HPVs show a greater propensity to recover over multiple cycles. Linear combinations of HPVs, which lie on the same planes in strain space as CV/HPV combinations, show no elevated residual strain accumulation compared to single HPV solutions. This can be seen in the flat trend in residual strain increasing secondary HPV fraction in Figure 4.5. Considering the rule of mixtures approach for CV and HPV mixtures for the mixing of two compatible HPVs, the limited change in residual strain is the result of two strain endpoints along the mixture line with the same (near zero) incompatibility with the parent austenite. Compare the flat trend of multiple HPV residual strain to the linear increase seen from adding an increasing amount of CVs (Figure 4.4) and it becomes clear that the potential complexity of the austenite-martensite interface is not a major contributor to increasing residual strain. The increase in residual strain from CV configured martensite can be attributed directly to the strain incompatibility of the CV phase rather than any tortuous interface it may form with the parent austenite phase.

In this section it was shown that points that transformed to correspondence variant configurations showed increased amounts of residual strain with cycling. These same points also showed large drops in the total volume fraction of martensite lost between the first and last superelastic cycles. Even points that deviated from a pure HPV configuration by a few percent showed a large martensite fraction loss compared to HPV-only configurations. The increase in residual strain was also shown to not be attributable to a more complex interface geometry between austenite and martensite, as there was no similar trend for multiple HPV configuration. In addition to identifying phase incompatibility as the primary cause of residual strain accumulation, the insensitivity of residual strain accumulation to multiple HPV solutions also indicates a minimal

penalty for a tortuous habit plane that flips between multiple orientations in an HPV combination, as long as the individual boundary segments maintain compatibility with the parent phase. Any deviation from a compatible mixture through the inclusion of CV configured martensite, however, becomes detrimental to later martensitic recovery as it induces increased residual strain and potentially retained martensite, as will be discussed in the next section.

SECTION 4.3: SHIFT IN TRANSFORMING VOLUME FRACTION

The saturation of residual strain and reduction of CV fraction with cycling corresponds to the macroscopic shakedown of the stress-strain response, and leads to a more uniform distribution of HPVs. The path of this transformation evolution can be traced across multiple loading cycles by tracking sets of points that transform to various volume fractions of HPV, CV, and austenite. By averaging the volume fraction change of many points with the same initial composition of transforming HPVs and CVs, trends in how the transforming volume fractions shift with cycling can become more apparent. The gathered data for an RD test was mapped onto an evenly distributed triangular mesh of representative phase fraction points through the Austenite-HPV-CV phase space based on the transformation volume fractions of the experiment's first cycle (Figure 4.3bc, Cycle 1). Points were assigned to the nearest mesh point and the average displacement of all points assigned to each mesh point defined the mesh displacement. While there are differences in where the final mixture of Austenite-HPV-CV mesh points lay for the history-free (Figure 4.3b) and history-dependent (Figure 4.3c) assumptions used to calculate the mesh point displacements, by cycle two these points have largely collapsed into configurations with a higher HPV fraction regardless of which history assumption is used. A stable configuration is reached by cycle five or six for both assumptions, corresponding with the shakedown of the macroscopic stress-strain curve and the saturation of the residual strain in the different martensite configurations (Figure 4.3a and

68

Figure 4.3d, respectively). Thus, shakedown can be attributed in part to a shift in transforming martensite volume fractions from configurations that are incompatible with the parent austenite to compatible configurations stabilized by plastic deformation and/or retained martensite.

As previously stated, the location of stable (shaken down) martensite depends on the amount of reorientation that is present in the local microstructure. If the history-free assumption is used in the fit (Figure 4.3b), which is analogous to an infinitely reorientable martensite configuration, all points collapse to a dense, primarily HPV configuration with a high transforming volume fraction of martensite. While the loss of recoverable strain in this configuration matches well with experimental results, it requires unreasonable assumptions about the residual strain field. Specifically the residual plastic deformation for the history free assumption just happens to take on values which perfectly account for the lost maximum strain from the initial configuration. This perfect match is required to account for the continued high level of strain memory seen in the maximum strain fields. Though unreasonably specific, this possibility cannot be discounted outright from this analysis. When considering a strict history assumption, one can limit transformation to the martensite variants present in cycle 1 (Figure 4.3c) which represents the strongest history dependent transformation bias and no cycle-to-cycle reorientation of martensite. This produces a more homogenous transformation, where every point containing some correspondence variant fraction collapses to a low-martensite fraction, primarily HPV configuration. Those points with no CV component, along the A↔HPV edge in Figure 4.3c, maintained their pure HPV character and slightly higher volume fractions of martensite. At the same time, the residual strain of this assumption can be mostly attributed to the lost transforming martensite fraction, removing the specific assumptions of large, coordinated plastic deformation required to explain the history free configurations. The true configuration of martensite in the

shaken down superelastic sample likely lies between these two extremes, but as the methods presented here can only give *a* best-fit configuration, the results ultimately depend on which phases are included in the fit.

As alluded to in the last paragraph, the degree of reorientability of martensite during cyclic superelastic transformation informs the source of residual strain. Depending on the use of either the history-free or strict-history assumption, either all or less than 20% of residual strain could be attributed to sources of residual strain other than martensite lock-in, respectively. Analysis using the history-free assumption of infinitely reorientable martensite resulted in a stable, shaken-down transformation configuration with a high volume fraction of actively transforming martensite. Using this assumption, significant recoverable martensite volume fraction was maintained throughout the specimen with cycling, and the maximum volume fraction loss of martensite was approximately 10% over ten cycles (see the phase distribution of cycle 10 in Figure 4.3b). The 10% maximum reduction was nominally uniform across all configurations of HPV and CV martensite. In comparison, the strict-history case – using the assumption of no martensite reorientation (Figure 4.3c) – resulted in the loss of approximately 50% of the martensite associated with non-HPV solutions and 30% of pure HPV configurations with cycling. When the decrease in strain associated with the loss of CV-bound martensite was considered in the history-free case, it was weakly correlated to measured residual strains. All points with a non-reoriented CV loss had, on average, approximately a 0.03 residual axial strain regardless of the total lost martensite transformation strain (Figure 4.6a). This means that other deformation mechanisms, namely plastic deformation, must be the cause of most to all of the residual strain if the history free assumption is true. The history-dependent loss in CV strain, however, accounted for 80% or more of the residual strain on a point by point basis (Figure 4.6b). In either case, the residual strain included

70

some locked-in martensite, which provided a lattice of configurations compatible with or included in the martensite of the first cycle. This residual lattice provided a low energy landscape that promoted that particular set of first cycle HPVs to repeatedly transform once the network was sufficiently established as seen in the correlation between the end of residual strain accumulation and the stability of the actively transforming martensite configuration around cycle 6 in figure 4.3. In this way, the residual strain network described here, whether it is primarily composed of retained martensite or a compatible dislocation network, represents the blueprint required to enforce repeated martensite transformation at the heart of macroscale strain memory.

A determination of how much residual strain is martensite and how much reorientation is present during superelastic cycling will require the further development of experimental capabilities. Diffraction-based analysis, which typically cannot measure local configurations over a wide area, could potentially be paired with the approaches used here to determine shifts in the martensite phase mixture. Tracking reorientation using diffraction-based methods would provide an additional input into the best fit model and allow the determination of the location of the shaken-down martensite configuration between the infinitely reorientable and strictly history dependent solutions. The residual strains measured in this work could then be ascribed to retained martensite or plasticity. Specifics of how this may be achieved will discussed in the final chapter of this dissertation.

SECTION 4.4: SUMMARY

A combined experimental and analytical approach was used to determine the likely configuration of transforming martensite during superelastic fatigue tests. It was found that in order to fit experimental measurements, lattice correspondence variants needed to be included in the solution set, even though specimens were not strained beyond the superelastic plateau. Residual

71

strain accumulated rapidly in areas that transformed into correspondence variants in the first cycle. Additionally, the accumulation of residual strain had a strong correlation with macroscopic shakedown; when residual strain accumulation slowed in the microstructure, macroscopic shakedown stabilized. Applying additional constraints during cycling resulted in two possible paths for residual strain accumulation. Without a penalty for reorientation, termed here as the history-free condition, only a small fraction of residual strain could be attributed to retained martensite. Enforcing a repeated transformation path as experimentally observed, termed here as the strict history condition, led to the attribution of a large fraction of residual strain to locked-in martensite. The results presented here could be improved with the development of experiments combining this novel methodology with approaches that can directly measure martensite reorientation over time.
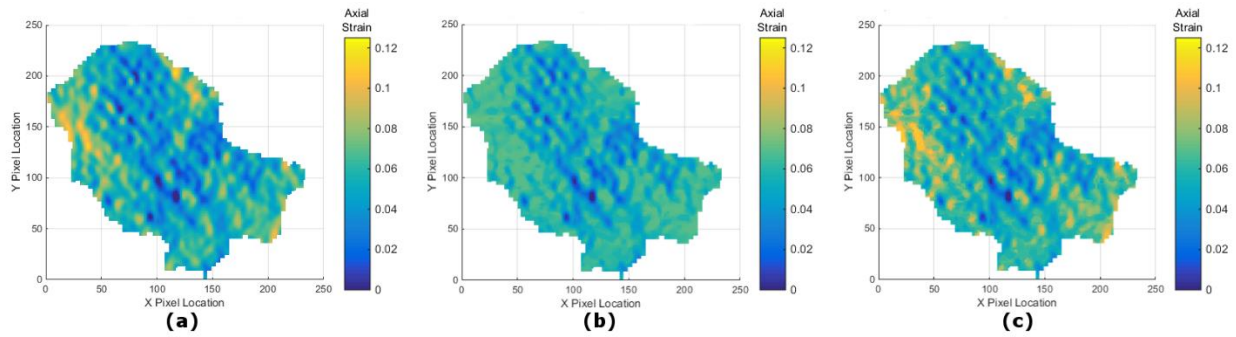
Figure 4.1: (a) Recovered axial strain measured during the first cycle of superelastic deformation in a single grain. (b) The best match of axial strain using only the HPV solutions available for the grain orientation. (c) The best match of axial strain using both the available HPV and CV solution sets. The vast improvement of the model fit after including the CV solutions is taken as strong evidence of reorientation of HPVs to their component CVs within the first superelastic cycle.
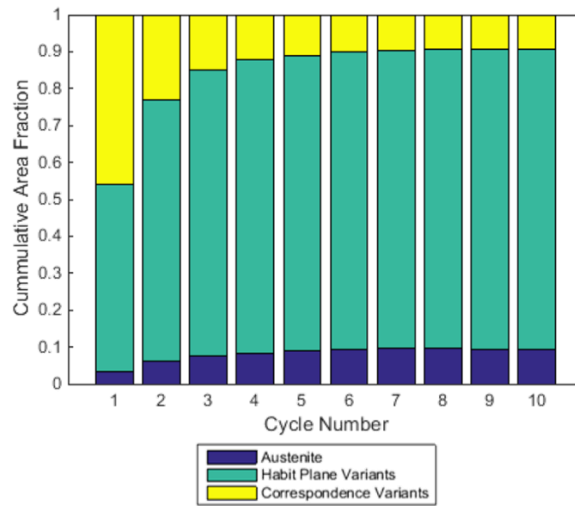
Figure 4.2: Distribution of phase fraction in the recovered strain fit for cycles 1-10. Note the stabilization of phase fraction around cycle 5 or 6 that correlates with the end of major shakedown of the macroscopic stress-strain response.
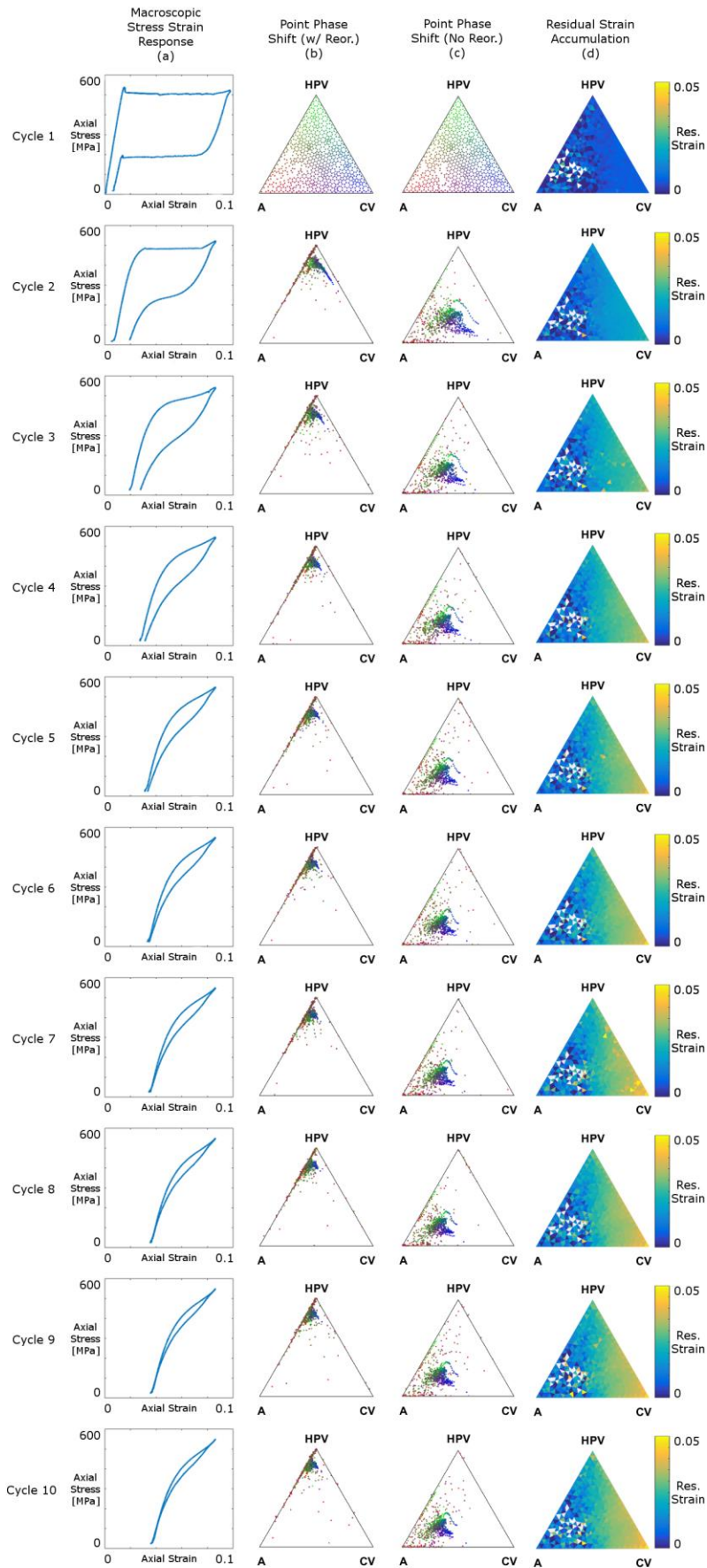
Figure 4.3: (a) The evolution of the macroscopic stress-strain response with superelastic cycling. (b/c) Tracking points with particular volume fractions in their initial recoverable transformation as they collapse to a more uniform HPV set with cycling. (d) The mean residual strain accumulated in the material based on the initial transformation volume fractions. Note the heightened accumulation of residual strain in material that initially transforms to high CV fractions.
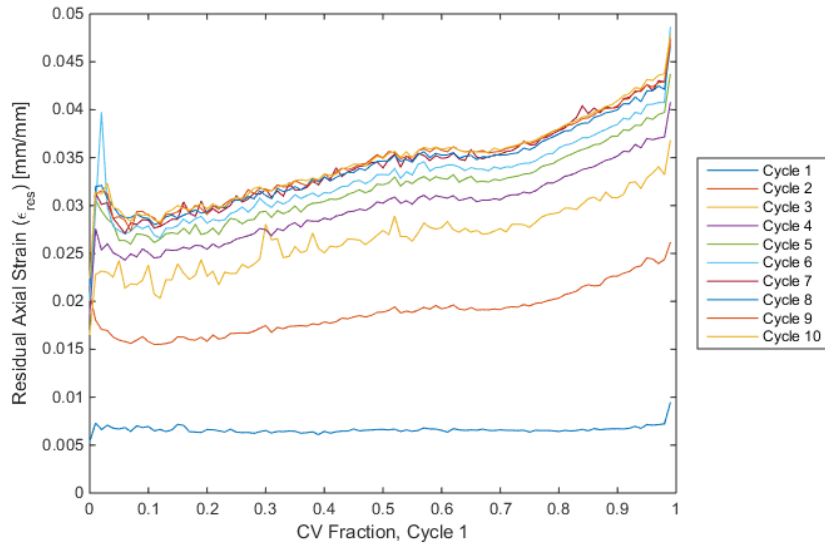
Figure 4.4: Mean residual strain accumulation in the sample over ten superelastic cycles as a function of the CV fraction of Cycle 1. This shows the linear accumulation of residual strain with increasing CV fraction in the initial martensite transformation configuration.
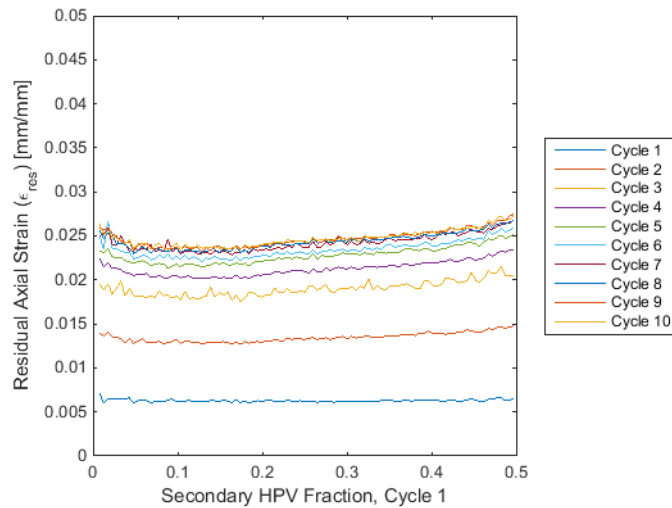
Figure 4.5: Mean residual strain accumulation in the sample over ten superelastic cycles as a function of the secondary HPV fraction in multi HPV configurations detected during Cycle 1. This shows the negligible increase in residual strain with multiple interacting HPV configurations.
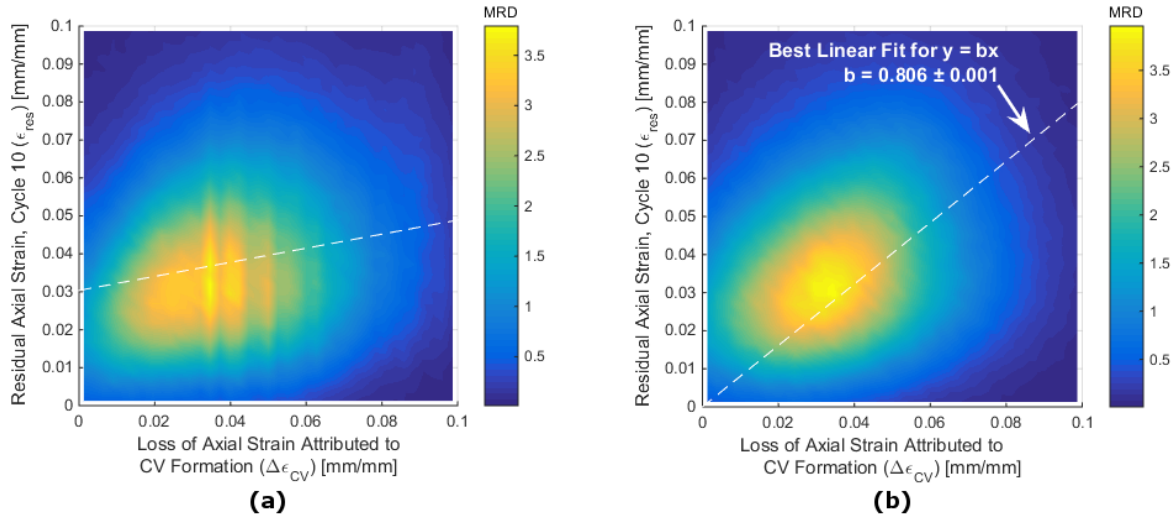
Figure 4.5: Relationship between loss of strain from correspondence variants in the case where (a) there is no penalty for reorientation and transformation history is not considered and (b) the previous transformation configuration fixes the martensite configurations available in subsequent cycle

CHAPTER 5: SUMMARY AND FUTURE WORK

This dissertation work investigates the role of martensite configuration on superelastic transformation, and shows that the secondary microstructure of martensite variants that forms during the initial cycle of superelastic transformation exerts a strong influence on the configuration and distribution of transformation in subsequent loading cycles. It has been shown for the first time that a hybrid structure of correspondence variants forms in addition to the previously predicted habit plane variants. Strain accumulation associated with correspondence variants is much different than that associated with habit plane variants, and their occurrence provides the basis for establishing a residual strain network that shapes future transformation. While further research is required to determine if the formation of correspondence variant networks can be fully predicted based on the primary microstructural features of the austenite polycrystal, tools for measuring their influence on strain accumulation during cyclic superelastic deformation are developed in this dissertation. The tools developed here have captured a novel transformation mode, the basic microstructural parameters that lead to its activation, and its impact on future transformation in the same microstructure.

SECTION 5.1: SUMMARY

This dissertation details the development of a suite of novel experimental and analytical techniques used to measure transformation strains at the microstructural length scale. Digital Image Correlation and its associated algorithms were adapted for use with Scanning Electron Microscopy in order to quantify the fine features of martensite transformation in superelastic nickel

titanium. The SEM-DIC technique required significant custom coding to remove the unique distortions of SEM imaging and new patterning methods were refined to leverage the full capabilities of SEM resolution and magnification. As shown throughout this dissertation, the level of resolution and coverage that this full-field technique provides subgrain details of local deformation, indicative of stress-induced martensitic transformation, across relatively large fields of view.

The SEM-DIC technique was used to simultaneously measure strains in the austenite and martensite phases at the sub-grain level across fields of view containing numerous grains, a first at the microstructural length scale. Combining this strain data with pre-test grain orientation measurements collected via EBSD enabled the quantification of martensite configuration maps using a custom algorithm which matched predicted transformation strains to the in plane strain components measured via SEM-DIC. Full details of this algorithm are provided in Chapter 2. It is evident from progressive transformation maps that martensite transformation is a heterogeneous, multistep process with a high degree of internal structure that is based on both the distribution and configuration of martensite variants in the transformed microstructure.

Combined SEM-DIC and EBSD was used to capture experimental evidence that crystal orientation alone does not predict transformation in a polycrystalline shape memory alloy. This assumption has been used previously in mean field theories, to varying degrees of success, to predict the macroscopic strains of superelastic material. [51–55] Here, because multiple strain field measurements could be made in each grain of the polycrystalline specimens during deformation, it was shown that neither the distribution of strains nor the average strain of individual grains matched single crystal results of the same orientation. Simply stated, similarly oriented grains do not transform similarly in polycrystals. Thus, models that solely rely on the orientation distribution

of a polycrystal do not accurately represent macroscale transformation, because grain orientation alone does not control transformation behavior. However, additional regressions that took into account additional microstructural features - such as grain size, surface distance to grain boundaries, or grain boundary misorientation - did not provide an improvement in predicting martensite transformation. The lack of transformation strain dependence on microstructural features is likely based in insufficient microstructural data, and will be addressed in the Future Work section of this chapter.

The analysis of local strain fields with respect to the local grain orientation also demonstrated that the transformation from austenite to martensite included singular correspondence variant (CV) configurations rather than just the habit plane variants (HPVs) previously thought to dominate early martensite transformation. The role of CV configurations had previously gone undetected, either from an inability to resolve martensite structures or because only the total distribution of martensite orientation across the entire polycrystals, rather than its local configuration, was captured. Using the local strain to determine martensite transformation configuration confirmed the presence of non-HPV martensite structures. The appearance of CVs in this work indicates that it is necessary to consider the inclusion of these incompatible martensite configurations in future models of martensite transformation. Additionally, the analysis of the underlying crystallography provided insight into the reasons that incompatible martensite configurations were formed in some regions and not others. Comparison and regressions of all data gathered for this dissertation work show a positive trend in selecting CV configurations over HPV configurations when the resolved shear along the HPV twinning planes increased. A similar trend in increased HPV formation was not seen for resolved stress along habit planes indicating

that the reorientation of martensite is a much more shear stress driven process than the initial formation of martensite twins.

The presence of CV martensite configurations in the initial superelastic transformation is critical to understanding the cyclic behavior of this material, because residual strain accumulates to a greater degree in CV configurations compared to the more compatible HPV configurations. Regardless of sample or grain orientation, there exists a roughly linear trend in accumulated residual strain with respect to the initial volume fraction of CV at each measurement point, and residual strain compounds with cycling, ultimately saturating when the macroscopic shakedown of the sample ceases. Residual strain networks likely serve as a blueprint for subsequent martensitic transformation, linking the initial transformation configuration to all future cycles and creating the previously observed strain memory effect. These networks serve as an information bridge in that they communicate the past transformation state to future cycles and bias the transformation to repeat. Therefore, understanding the microstructural features which may bias transformation to CV configurations is critical in understanding the accumulation of fatigue damage in polycrystalline nickel titanium and the repeatability of martensite transformation with cycling.

SECTION 5.2: FUTURE WORK

Further work to expand this dissertation research is required to gain a richer understanding of martensite transformation in polycrystalline superelastic shape memory alloys. Primarily, this will involve integrating additional experimental techniques to the methodology used here to augment the available data set and limit the available degrees of freedom which required assumptions in this work. The incorporation of additional experimental tools can potentially expand the surface methods used here into fully 3-D analysis techniques. Experimental methods

80

exist that can be seamlessly integrated into those used here to provide 3-D input to more accurately analyze the interactions at work during martensitic transformation. Diffraction techniques [107,109–111] can provide additional information about the total martensite configuration distribution, which can eliminate some of the assumptions used here about the repeatability of martensite transformation and the nature of residual strain. Additionally, both destructive [112,113] and non-destructive [114,115] methods can be used to obtain the full 3-D microstructure and provide more complete inputs to logistic regression models, in order to improve the characterization of microstructural influences of transformation completeness and configuration. Finally, the mechanistic interactions between martensitic transformation, plasticity, and microstructural features require greater scrutiny, which can be provided by careful post-mortem analysis with high resolution transmission electron microscopy.

The 2-D measurements of SEM-DIC mean that only three of the six independent strain components were included in the martensite match. This leads to redundancy in the 3-D projection of these 6-D objects in the matching algorithm. With the current technique there is no way to separate them without making assumptions on the existence of compatibility with other present phases. However, the particular species of martensite present in each of these redundant variants provides additional information with which to identify them. Neutron diffraction data [107,109,110] or high resolution X-ray diffraction [111] can provide a total sum of martensite species in the transformed polycrystal while running a simultaneous DIC test. This martensite orientation distribution can then be used as an input to the martensite matching algorithm as either a weighting function to preference the matching of certain variants or as a hard stop to limit the number of times a particular variant can appear in the solution. The addition of diffraction data

would provide a limit to the configuration of martensite in the transformed microstructure and removes degrees of freedom in the matching algorithm.

In addition to providing an input to the matching algorithm directly, supplementary diffraction studies can provide information about the amount of martensite reorientation and retention taking place during superelastic cycling. In Chapter 4, the analysis of the shaken down martensite configuration depended on whether the martensite transformation had a history dependence or if each cycle took an independent transformation path. As with the redundancy in the individual martensite projections, the redundancy in these solutions was due to only using a projection of the full strain tensor. In this case, what is needed to move past a reliance on assumptions is the relative difference in martensite orientation for a representative test, rather than the absolute orientation for a concurrent diffraction and DIC experiment. From previous strain memory experiments and observations of a high degree of strain memory in the maximum local transformation strain, it can be expected that such a test would show a history-dependent, largely non-reorienting set of martensite variants reappearing each cycle. However, the perfect history assumption used in this dissertation analysis does not fully match the experimental results. Therefore, direct experimental evidence is required to determine to what degree martensite reorientation is taking place with cycling. With supplemental information about the relative ease of reorientation for the actively transforming superelastic martensite, as well as measurements of any retained martensite, the assumptions of Chapter 4 can be replaced with empirically derived limits on martensite reorientation. This would allow determination of whether retained strain in superelastic polycrystals is principally made up of retained martensite or plastic deformation, which remains an open question.

Diffraction experiments also provide an avenue to generate the necessary 3-D microstructure to more accurately determine if there are any microstructural features which bias martensitic transformation. The regressions performed in this work were limited to microstructural features that could be derived from two-dimensional surface measurements obtained by EBSD. Synchrotron XRD scans [114,115] can provide non-destructive orientation measurements of subsurface grains prior to deformation to relate the full three dimensional microstructure to surface strains. This can be a costly and time consuming technique, but given the relatively small area which needs to be characterized it may be feasible to perform for SEM-DIC level experiments. Alternatively, destructive serial sectioning and EBSD [112,113] can gather equivalent data necessary to reconstruct the microstructure after a DIC test has been performed. Both techniques provide the true grain boundary distance, grain boundary orientation and misorientation, triple point locations, and all other spatially dependent microstructural features for complete regression analysis.

Lastly, in addition to validating assumptions made in this work or using other experimental techniques to generate more detailed microstructures for regression analysis, there is work to be done in analyzing the structure of residual strain in polycrystals. If diffraction experiments indicate the residual strain is a mixture of residual martensite and plasticity, there is then a question of how those two deformation mechanisms interact to stabilize martensite against reverse transformation. Previous TEM imaging of nickel titanium [25,36,57,116,117] has been able to image stabilized martensite structures in reference to the surrounding plastic deformation. However, these images do not come at the benefit of knowing the complete strain history of the imaged area. Given the local strain measurement of SEM-DIC, it should be possible to select a retained martensite lath and, knowing its orientation relative to the surface due to the improved martensite matching

algorithm, extract a representative section using Focused Ion Beam machining. Many samples could be pulled from a single polycrystal to provide a large sampling of how different martensite variants and their surrounding plastic zones interact to form stabilized martensite. Alternatively, samples could be machined from the same specimen periodically while it is cycled to see how dislocation structures develop around martensite laths of similar character. In either case, higher resolution microscopy will allow for the examination of the mechanistic interaction between martensite and plasticity, and expand upon this works early understanding of residual strain accumulation in particular martensite structures.

SECTION 5.3: CONCLUSIONS

For the first time a single measurement technique was used to simultaneously track the transformation to and recovery of martensite in a polycrystalline specimen. These observations provide new details on how the macroscopic martensite band progresses through a polycrystals and how that martensite is configured in the transformed martensite band. Previously unobserved correspondence variant configurations of martensite were found to readily form in the polycrystalline specimens. A positive relationship between the resolved shear stress on twin planes and the appearance of these CV configurations was also identified using logistic regression. Cycling polycrystalline specimens caused those areas which primarily transformed to CV configurations to accumulate an increased amount of residual strain. This residual strain network persisted and intensified with cycling, serving as a blueprint for subsequent transformation. While the interaction between martensite, plasticity, and polycrystalline microstructures requires more work to fully characterize, this dissertation work represents a foray into understanding the complex interactions taking place when cycling superelastic material.

REFERENCES

[1]   Bhattacharya K. Microstructure of Martensite: Why it forms and how it gives rise to the shape memory effect. New York: Oxford University Press Inc.; 2003.

[2]   Otsuka K, Ren X. Physical metallurgy of Ti–Ni-based shape memory alloys. Prog Mater Sci 2005;50:511–678.

[3]   Robertson SW, Pelton AR, Ritchie RO. Mechanical fatigue and fracture of Nitinol. Int Mater Rev 2011;57:1–36.

[4]   Shaw JA, Kyriakides S. Thermomechanical aspects of NiTi. J Mech Phys Solids 1995;43:1243–81.

[5]   Shaw JA, Kyriakides S. On the nuecleation transformation and propogation of phase fronts in a NiTi alloy. Acta Mater 1997;45:683–700.

[6]   Kim K, Daly SH. The effect of texture on stress-induced martensite formation in nickel–titanium. Smart Mater Struct 2013;22:075012.

[7]   Lackmann J, Niendorf T, Maxisch M, Grundmeier G, Maier HJ. High-resolution in-situ characterization of the surface evolution of a polycrystalline NiTi SMA-alloy under pseudoelastic deformation. Mater Charact 2011;62:298–303.

[8]   Daly SH, Ravichandran G, Bhattacharya K. Stress-induced martensitic phase transformation in thin sheets of Nitinol. Acta Mater 2007;55:3593–600.

[9]   Murasawa G, Kitamura K, Yoneyama S, Miyazaki S, Miyata K, Nishioka A, et al. Macroscopic stress–strain curve, local strain band behavior and the texture of NiTi thin sheets. Smart Mater Struct 2009;18:055003.

[10]   Gall K, Tyber J, Brice V, Frick CP, Maier HJ, Morgan N. Tensile deformation of NiTi wires. J Biomed Mater Res A 2005;75:810–23.

[11]   Churchill CB, Shaw JA, Iadicola MA. Tips and Tricks for Characterizing Shape Memory Alloy Wire: Part 2-Fundamental Isothermal Responses. Exp Tech 2009;33:51–62.

[12]   DesRoches R, McCormick J, Delemont M. Cyclic Properties of Superelastic Shape Memory Alloy Wires and Bars. J Struct Eng 2004;130:38–46.

[13]   Churchill CB, Shaw JA, Iadicola MA. Tips and Tricks for Characterizing Shape Memory Alloy Wire: Part 3-Localization and Propagation Phenomena. Exp Tech 2009;33:70–8.

[14]   Kim K, Daly SH. Martensite Strain Memory in the Shape Memory Alloy Nickel-Titanium Under Mechanical Cycling. Exp Mech 2010;51:641–52.

[15]   Maletta C, Sgambitterra E, Furgiuele F, Casati R, Tuissi A. Fatigue properties of a pseudoelastic NiTi alloy: Strain ratcheting and hysteresis under cyclic tensile loading. Int J Fatigue 2014;66:78–85.

[16]   Olbricht J, Yawny A, Pelegrina JL, Dlouhy A, Eggeler G. On the Stress-Induced Formation of R-Phase in Ultra-Fine-Grained Ni-Rich NiTi Shape Memory Alloys. Metall Mater Trans A 2011;42:2556–74.

[17]   Mao SC, Luo JF, Zhang Z, Wu M, Liu Y, Han XD. EBSD studies of the stress-induced B2–B19′ martensitic transformation in NiTi tubes under uniaxial tension and compression. Acta Mater 2010;58:3357–66.

[18]   Reedlunn B, Churchill CB, Nelson EE, Shaw JA, Daly SH. Tension, compression, and bending of superelastic shape memory alloy tubes. J Mech Phys Solids 2014;63:506–37.

[19]   Bechle NJ, Kyriakides S. Localization in NiTi tubes under bending. Int J Solids Struct 2014;51:967–80.

[20]   Wagner MF-X, Schaefer A. Macroscopic versus local strain rates during tensile testing of pseudoelastic NiTi. Scr Mater 2010;63:863–6.

[21]   He YJ, Sun QP. Rate-dependent domain spacing in a stretched NiTi strip. Int J Solids Struct 2010;47:2775–83.

[22]   Brinson LC. Stress-induced transformation behavior of a polycrystalline NiTi shape memory alloy: micro and macromechanical investigations via in situ optical microscopy. J Mech Phys Solids 2004;52:1549–71.

[23]   Kimiecik MG, Jones JW, Daly SH. Quantitative studies of microstructural phase transformation in Nickel–Titanium. Mater Lett 2013;95:25–9.

[24]   Kimiecik MG, Jones JW, Daly SH. Quantitative Analysis of Phase Transformation in Ni-Ti Shape Memory Alloys. Adv Mater Process 2013;21:21–5.

[25]   Ye J, Mishra RK, Pelton AR, Minor AM. Direct observation of the NiTi martensitic phase transformation in nanoscale volumes. Acta Mater 2010;58:490–8.

[26]   Barney M, Xu D, Robertson SW, Schroeder V, Ritchie RO, Pelton AR, et al. Impact of thermomechanical texture on the superelastic response of nitinol implants. J Mech Behav Biomed Mater 2011;4:1431–9.

[27] Mehta A, Gong X-Y, Imbeni V, Pelton AR, Ritchie RO. Understanding the deformation and fracture of nitinol endovascular stents using in situ synchrotron X-ray microdiffraction. Adv Mater 2007;19:1183–6.

[28] Robertson SW, Gong X-Y, Ritchie RO. Effect of product form and heat treatment on the crystallographic texture of austenitic Nitinol. J Mater Sci 2006;41:621–30.

[29] Knowles K, Smith D. The crystallography of the martensitic transformation in equiatomic Nickel-Titanium. Acta Metall 1980;29:101–10.

[30] Matsumoto O, Miyazaki S, Otsuka K, Tamura H. Crystallography of martensitic transformation in Ti-Ni single crystals. Acta Metall 1987;35:2137–44.

[31] Hane K, Shield TW. Microstructure in the cubic to monoclinic transition in titanium–nickel shape memory alloys. Acta Mater 1999;47:2603–17.

[32] Bhattacharya K, Kohn RV. Elastic Energy Minimization and the Recoverable Strains of Polycrystalline Shape-Memory Materials. Arch Ration Mech Anal 1997;139:99–180.

[33] Miyazaki S, Kimura S, Otsuka K, Suzuki T. The habit plane and transformation strains associated with the martensitic transformation in Ti-Ni single crystals. Scr Metall 1984;18:883–8.

[34] Gall K, Dunn M, Liu Y, Labossiere P, Sehitoglu H, Chumlyakov Y. Micro and macro deformation of single crystal NiTi. J Eng Mater Technol 2002;124:238.

[35] Gall K, Sehitoglu H, Chumlyakov Y, Kireeva I V. Tension-compression asymmetry of the stress-strain response in aged single crystal and polycrystalline NiTi. Acta Mater 1999;47:1203–17.

[36] Norfleet D, Sarosi P, Manchiraju S, Wagner MF-X, Uchic MD, Anderson PM, et al. Transformation-induced plasticity during pseudoelastic deformation in Ni–Ti microcrystals. Acta Mater 2009;57:3549–61.

[37] Patoor E, Lagoudas DC, Entchev P, Brinson LC, Gao X. Shape memory alloys, Part I: General properties and modeling of single crystals. Mech Mater 2006;38:391–429.

[38] Sehitoglu H, Karaman I, Anderson R, Zhang X, Gall K, Maier HJ, et al. Compressive response of NiTi single crystals. Acta Mater 2000;48:3311–26.

[39] Manjeri R, Qiu S, Mara N, Misra A, Vaidyanathan R. Superelastic response of [111] and [101] oriented NiTi micropillars. J Appl Phys 2010;108:023501.

[40] Frick CP, Orso S, Arzt E. Loss of pseudoelasticity in nickel–titanium sub-micron compression pillars. Acta Mater 2007;55:3845–55.

[41]   Frick CP, Lang T, Spark K, Gall K. Stress-induced martensitic transformations and shape memory at nanometer scales. Proc. Int. Conf. Shape Mem. Superelastic Technol., 2006, p. 99–111.

[42]   Frick CP, Clark BG, Orso S, Sonnweber-Ribic P, Arzt E. Orientation-independent pseudoelasticity in small-scale NiTi compression pillars. Scr Mater 2008;59:7–10.

[43]   Miyazaki S, No V, Kitamura K, Khantachawana A, Hosoda H. Texture of Ti–Ni rolled thin plates and sputter-deposited thin films. Int J Plast 2000;16:4–8.

[44]   Yuan W, Yi S. Pseudo-elastic strain estimation of textured TiNi shape memory alloys. Mater Sci Eng A 1999;271:439–48.

[45]   Inoue H, Miwa N, Inakazu N. Texture and shape memory strain in TiNi alloy sheets. Acta Mater 1996;44:4825–34.

[46]   Shu Y, Bhattacharya K. The influence of texture on the shape-memory effect in polycrystals. Acta Mater 1998;46:5457–73.

[47]   Šittner P, Novák V. Anisotropy of martensitic transformations in modeling of shape memory alloy polycrystals. Int J Plast 2000;16:1243–68.

[48]   Bhattacharya K, Schlömerkemper A. Stress-Induced Phase Transformations in Shape-Memory Polycrystals. Arch Ration Mech Anal 2009;196:715–51.

[49]   Miyazaki S, Ishida A. Martensitic transformation and shape memory behavior in sputter-deposited TiNi-base thin films. Mater Sci Eng A 1999;273-275:106–33.

[50]   Bhattacharya K, Kohn RV. Symmetry, texture and the recoverable strain of shape-memory polycrystals. Acta Mater 1996;44:529–42.

[51]   Lagoudas DC, Entchev P, Popov P, Patoor E, Brinson LC, Gao X. Shape memory alloys, Part II: Modeling of polycrystals. Mech Mater 2006;38:430–62.

[52]   Lagoudas DC, Hartl D, Chemisky Y, Machado L, Popov P. Constitutive model for the numerical analysis of phase transformation in polycrystalline shape memory alloys. Int J Plast 2012;32-33:155–83.

[53]   Richards A, Lebensohn R, Bhattacharya K. Interplay of martensitic phase transformation and plastic slip in polycrystals. Acta Mater 2013;61:4384–97.

[54]   Shaw JA. Simulations of localized thermo-mechanical behavior in a NiTi shape memory alloy. Int J Plast 2000;16:541–62.

[55]   Gall K, Lim T, McDowell D, Sehitoglu H. The role of intergranular constraint on the stress-induced martensitic transformation in textured polycrystalline NiTi. Int J 2000;16:1189–214.

[56]   Yamamoto H, Taya M, Liang Y, Namli OC, Saito M. Fatigue properties of NiTi shape-memory alloy thin plates 2013;8689:86890S.

[57]   Pelton AR. Nitinol Fatigue: A Review of Microstructures and Mechanisms. J Mater Eng Perform 2011;20:613–7.

[58]   Eggeler G, Hornbogen E, Yawny A, Heckmann A, Wagner MF-X. Structural and functional fatigue of NiTi shape memory alloys. Mater Sci Eng A 2004;378:24–33.

[59]   Kang G. Advances in transformation ratcheting and ratcheting-fatigue interaction of NiTi shape memory alloy. Acta Mech Solida Sin 2013;26:221–36.

[60]   Kumar PK, Caer C, Atkinson G, Patoor E, Lagoudas DC. The influence of stress and temperature on the residual strain generated during pseudoelastic cycling of NiTi SMA wires 2011;7978:79781E – 79781E – 9.

[61]   Kang G, Kan Q, Qian L, Liu Y. Ratchetting deformation of super-elastic and shape-memory NiTi alloys. Mech Mater 2009;41:139–53.

[62]   Pelton AR, Schroeder V, Mitchell MR, Gong X-Y, Barney M, Robertson SW. Fatigue and durability of Nitinol stents. J Mech Behav Biomed Mater 2008;1:153–64.

[63]   Shaw JA. Material Instabilites in a Nickel-Titanium Shape Memory Alloy. University of Texas, 1997.

[64]   Stebner A, Vogel SC, Noebe RD, Sisneros TA, Clausen B, Brown DW, et al. Micromechanical quantification of elastic, twinning, and slip strain partitioning exhibited by polycrystalline, monoclinic nickel–titanium during large uniaxial deformations measured via in-situ neutron diffraction. J Mech Phys Solids 2013;61:2302–30.

[65]   Ortin J, Planes A, Delaey L. Hysteresis in shape-memory materials. Sci Hysteresis 2006;3:467–553.

[66]   Rao A, Ruimi A, Srinivasa AR. Internal loops in superelastic shape memory alloy wires under torsion – Experiments and simulations/predictions. Int J Solids Struct 2014;51:4554–71.

[67]   Frick CP, Clark BG, Schneider AS, Maaß R, Petegem S Van, Swygenhoven H Van. On the plasticity of small-scale nickel–titanium shape memory alloys. Scr Mater 2010;62:492–5.

[68]   Pfetzing-Micklich J, Ghisleni R, Simon T, Somsen C, Michler J, Eggeler G. Orientation dependence of stress-induced phase transformation and dislocation plasticity in NiTi shape memory alloys on the micro scale. Mater Sci Eng A 2012;538:265–71.

[69]   Bowers ML, Chen X, De Graef M, Anderson PM, Mills MJ. Characterization and modeling of defects generated in pseudoelastically deformed NiTi microcrystals. Scr Mater 2014;78-79:69–72.

[70]   Song Y, Chen X, Dabade V, Shield TW, James RD. Enhanced reversibility and unusual microstructure of a phase-transforming material. Nature 2013;502:85–8.

[71]   Madangopal K. The self accommodating martensitic microstructure of NiTi shape memory alloys. Acta Mater 1997;45:5347–65.

[72]   Miyazaki S, Otsuka K, Wayman CM. The shape memory mechanism associated with the martensitic transformation in Ti-Ni alloys—I. Self-accommodation. Acta Metall 1989;37:1873–84.

[73]   Miyazaki S, Otsuka K, Wayman CM. The shape memory mechanism associated with the martensitic transformation in Ti-Ni alloys—II. Variant coalescence and shape recovery. Acta Metall 1989;37:1885–90.

[74]   Chen X, Srivastava V, Dabade V, James RD. Study of the cofactor conditions: Conditions of supercompatibility between phases. J Mech Phys Solids 2013;61:2566–87.

[75]   Shi H, Delville R, Srivastava V, James RD, Schryvers D. Microstructural dependence on middle eigenvalue in Ti–Ni–Au. J Alloys Compd 2014;582:703–7.

[76]   Delville R, Kasinathan S, Zhang Z, Humbeeck J Van, James RD, Schryvers D. Transmission electron microscopy study of phase compatibility in low hysteresis shape memory alloys. Philos Mag 2010;90:177–95.

[77]   Pelton AR. Personal Correspondance 2013.

[78]   Pelton AR, Dicello J, Miyazaki S. Optimisation of processing and properties of medical grade Nitinol wire. Minim Invasive Ther Allied Technol 2000;9:107–18.

[79]   Gall K, Sehitoglu H, Chumlyakov Y. The influence of aging on critical transformation stress levels and martensite start temperatures in NiTi. Part I: Aged microstructure and micro-mechanical modeling. J Eng Mater Technol 1999;121:19–27.

[80]   Gall K, Sehitoglu H, Chumlyakov Y. The influence of aging on critical transformation stress levels and martensite start temperatures in NiTi. Part II: Discussion of experimental results. J Eng Mater Technol 1999;121:28–37.

[81] Michutta J, Somsen C, Yawny A, Dlouhy A, Eggeler G. Elementary martensitic transformation processes in Ni-rich NiTi single crystals with Ni4Ti3 precipitates. Acta Mater 2006;54:3525–42.

[82] Tirry W, Schryvers D. Quantitative determination of strain fields around Ni4Ti3 precipitates in NiTi. Acta Mater 2005;53:1041–9.

[83] Baxevanis T, Cox A, Lagoudas DC. Micromechanics of precipitated near-equiatomic Ni-rich NiTi shape memory alloys. Acta Mech 2014;225:1167–85.

[84] Zhou N, Shen C, Wagner MF-X, Eggeler G, Mills MJ, Wang YQ. Effect of Ni4Ti3 precipitation on martensitic transformation in Ti-Ni. Acta Mater 2010;58:6685–94.

[85] Cox A, Baxevanis T, Lagoudas DC. Numerical Evaluation of the Effect of Ni4Ti3 Precipitates on the overall Thermo-Mechanical Response of NiTi Shape Memory Alloys. Proc. ASME 2013 Conf. Smart Mater. Adapt. Struct. Intell. Sysems, 2013, p. 1–7.

[86] Pelton AR, Dicello J, Miyazaki S. Optimization of processing and properties of medical-grade nitinol wire. Minim Invasive Ther Allied Technol 2000;9:107–18.

[87] Kammers AD, Daly SH. Digital image correlation under scanning electron microscopy: Methodology and validation. Exp Mech 2013;53:1743–61.

[88] Kammers AD, Daly SH. Self-assembled nanoparticle surface patterning for improved digital image correlation in a scanning electron microscope. Exp Mech 2013;53:1333–41.

[89] Sutton MA, Li N, Joy DC, Reynolds AP, Li X. Scanning electron microscopy for quantitative small and large deformation measurements Part I: SEM imaging at magnifications from 200 to 10,000. Exp Mech 2007;47:775–87.

[90] Sutton MA, Li N, Garcia D, Cornille N, Orteu J-J, McNeill SR, et al. Metrology in a scanning electron microscope: theoretical developments and experimental validation. Meas Sci Technol 2006;17:2613–22.

[91] Schreier HW, Orteu J-J, Sutton MA. Image Correlation for Shape, Motion and Deformation Measurements. Boston, MA: Springer US; 2009.

[92] Tian Q, Huhns MN. Algorithms for subpixel registration. Comput Vision, Graph Image Process 1986;35:220–33.

[93] Sutton MA, Li N, Garcia D, Cornille N, Orteu J-J, McNeill SR, et al. Scanning electron microscopy for quantitative small and large deformation measurements Part I: SEM imaging at magnifications from 200 to 10,000. Exp Mech 2007;47:789–804.

[94] Gall K, Sehitoglu H. The role of texture in tension-compression asymmetry in polycrystalline NiTi. Int J Plast 1999;15:69–92.

[95] Ball J, James RD. Fine phase mixtures as minimizers of energy. Anal Contin Mech 1989.

[96] James G, Witten D, Hastie T, Tibshirani R. An Introduction to Statistical Learning with Applications in R. 2013.

[97] Liu Y, Xie ZL. Twinning and detwinning of 011 type II twin in shape memory alloy. Acta Mater 2003;51:5529–43.

[98] Knowles KM. A high-resolution electron microscope study of nickel-titanium martensite. Philos Mag A 1982;45:357–70.

[99] Ezaz T, Sehitoglu H. Type II detwinning in NiTi. Appl Phys Lett 2011;98:139–42.

[100] Buchheit T, Kumpf S, Wert J. Modeling the stress-induced transformation behavior of shape memory alloy single crystals. Acta Metall Mater 1995;43:4189–99.

[101] Savi M, Paiva A, Baeta-Neves A, Pacheco P. Phenomenological modeling and numerical simulation of shape memory alloys: A thermo-plastic-phase transformation coupled model. J Intell Mater Syst Struct 2002;13:261–73.

[102] Ren W, Li H, Song G. Phenomenological modeling of the cyclic behavior of superelastic shape memory alloys. Smart Mater Struct 2007;16:1083–9.

[103] Arghavani J, Auricchio F, Naghdabadi R, Reali A, Sohrabpour S. A 3-D phenomenological constitutive model for shape memory alloys under multiaxial loadings. Int J Plast 2010;26:976–91.

[104] Bouvet C, Calloch S, Lexcellent C. A phenomenological model for pseudoelasticity of shape memory alloys under multiaxial proportional and nonproportional loadings. Eur J Mech - A/Solids 2004;23:37–61.

[105] Thamburaja P. A finite-deformation-based phenomenological theory for shape-memory alloys. Int J Plast 2010;26:1195–219.

[106] Buchheit T, Wert J. Modeling the effects of stress state and crystal orientation on the stress-induced transformation of NiTi single crystals. Metall Mater Trans A 1994;25:2383–9.

[107] Stebner A, Paranjape H, Clausen B, Brinson LC, Pelton AR. In-Situ Neutron Diffraction Studies of Large Monotonic Deformations of Superelastic Nitinol. Shape Mem Superelastcity 2015.

[108] Chluba C, Ge W, Lima de Miranda R, Strobel J, Kienle L, Quandt E, et al. Ultralow-fatigue shape memory alloy films. Science (80-) 2015;348:1004–7.

[109] Stebner A, Gao X, Brown DW, Brinson LC. Neutron diffraction studies and multivariant simulations of shape memory alloys: Empirical texture development–mechanical response relations of martensitic nickel–titanium. Acta Mater 2011;59:2841–9.

[110] Pelton AR, Clausen B, Stebner A. In-situ Neutron Diffraction Studies of Increasing Tension Pre-Strain Amplitudes of Superelastic Nitinol. Shape Mem Superelastcity 2015.

[111] Raghunathan SL, Azeem MA, Collins D, Dye D. In situ observation of individual variant transformations in polycrystalline NiTi. Scr Mater 2008;59:1059–62.

[112] Rowenhorst DJ, Gupta A, Feng CR, Spanos G. 3D Crystallographic and morphological analysis of coarse martensite: Combining EBSD and serial sectioning. Scr Mater 2006;55:11–6.

[113] Groeber M, Haley BK, Uchic MD, Dimiduk DM, Ghosh S. 3D reconstruction and characterization of polycrystalline microstructures using a FIB-SEM system. Mater Charact 2006;57:259–73.

[114] Liu W, Ice GE, Larson BC, Yang W, Tischler JZ, Budai JD. The three-dimensional X-ray crystal microscope: A new tool for materials characterization. Metall Mater Trans A 2004;35:1963–7.

[115] Larson BC, Yang W, Ice GE, Budai JD, Tischler JZ. Three-dimensional X-ray structural microscopy with submicrometre resolution. Nature 2002;415:887–90.

[116] Manchuraju S, Kroeger A, Somsen C, Dlouhy A, Eggeler G, Sarosi P, et al. Pseudoelastic deformation and size effects during in situ transmission electron microscopy tensile testing of NiTi. Acta Mater 2012;60:2770–7.

[117] Wang S, Tsuchiya K, Wang L, Umemoto M. Deformation Mechanism and Stabilization of Martensite in TiNi Shape Memory Alloy. J Mater Sci Technol 2010;26:936–40.